Mechanochemical upcycling of spent $LiCoO_2$ to new $LiNi_{0.80}Co_{0.15}Al_{0.05}O_2$ battery: An atom economy strategy

Jiadong Yu[a] (ID), Ju Li[b,c] (ID), Shang Zhang[a], Fan Wei[a] (ID), Yanjun Liu[a] (ID), and Jinhui Li[a,1] (ID)

The use of strong acids and low atom efficiency in conventional hydrometallurgical recycling of spent lithium-ion batteries (LIBs) results in significant secondary wastes and CO_2 emissions. Herein, we utilize the waste metal current collectors in spent LIBs to promote atom economy and reduce chemicals consumption in a conversion process of spent $Li_{1-x}CoO_2$ (LCO) → new $LiNi_{0.80}Co_{0.15}Al_{0.05}O_2$ (NCA) cathode. Mechanochemical activation is employed to achieve moderate valence reduction of transition metal oxides ($Co^{3+} \to Co^{2+,3+}$) and efficient oxidation of current collector fragments ($Al^0 \to Al^{3+}$, $Cu^0 \to Cu^{1+,2+}$), and then due to stored internal energy from ball-milling, the leaching rates of Li, Co, Al, and Cu in the ≤4 mm crushed products uniformly approach 100% with just weak acetic acid. Instead of corrosive precipitation reagents, larger Al fragments (≥4 mm) are used to control the oxidation/reduction potential (ORP) in the aqueous leachate and induce the targeted removal of impurity ions (Cu, Fe). After the upcycling of NCA precursor solution to NCA cathode powders, we demonstrate excellent electrochemical performance of the regenerated NCA cathode and improved environmental impact. Through life cycle assessments, the profit margin of this green upcycling path reaches about 18%, while reducing greenhouse gas emissions by 45%.

spent lithium-ion batteries | recycling | circular economy | atom economy | e-waste

While lithium-ion batteries (LIBs) have revolutionized consumer electronics, transportation, and energy markets, millions of tons of important metal resources are embedded in municipal waste streams after the LIBs fail (1–3). Ill disposal of spent LIBs causes heavy pollution and fire accidents (4). As a typical anthropogenic mineral, the concentration of key metals in spent LIBs is 3 to 10 times that of natural mineral concentrates, and thus, its reuse will improve the supply security of lithium and cobalt resources (5, 6). Furthermore, the recycling of spent LIBs can reduce CO_2 emissions coming from the mining and smelting of primary mineral resources, thereby contributing to the goal of carbon neutrality.

The recycling and upcycling of spent LIBs are under heavy development (7–9). Researchers are no longer just satisfied with a metal recovery rate greater than 98%, but are also beginning to care about how to reduce the consumption of chemicals in the recovery process in order to reduce the environmental footprint while improving the profitability (10–12). Thus, in situ recycling methods have emerged, namely, using physicochemical means to stimulate the redox potential of the inherent components of spent LIBs to enhance the dissolution efficiency of transition metal (13, 14). Spent LIBs are mainly composed of transition metal oxide cathode, graphite anode, current collectors (Cu/Al foils), polymer separators, and steel shells (15). Among them, zero-valent metals such as Fe shells, Al foils, and Cu foils, are natural reducing agents that have been used to develop in situ recycling technology (16, 17). Joulie et al. proposed that the current collectors can act as reducing agents to enhance the leaching of cathode materials of spent ternary LIBs, and thermodynamic analysis was performed (18). Peng et al. also found that a dual reducing agent system composed of Cu foils and Fe^{2+}/Fe^{3+} impurities can significantly increase the leaching rate of Li and Co, from 80% to about 100% (19). Fe^{2+} ion has a lower reduction potential and can reduce the $Li_{1-x}CoO_2$ (LCO) cathodes, while the oxidized Fe^{3+} iron is reduced by Cu foils, so Fe^{2+} ion in the system can play a cyclic role of soluble redox mediator (20). Although Al^0 has a stronger reducing ability to directly reduce the cathode materials without the participation of iron ions, it is easy to react with acid to generate H_2, which not only increases the consumption of harsh H_2SO_4, but also poses the risk of fire and explosion. On the other hand, Al^0 production is energy and CO_2 intensive. If Al foils can be used as a reducing agent to replace hydrogen peroxide, the additional environmental impact of the subsequent regeneration of waste foils and the production process of traditional reducing agent can be reduced by 13.8 ton of CO_2 per ton Al (20, 21). Therefore, the in situ utilization of Al^0 is very important for carbon

Significance

The rapid expansion of the electric vehicle market generates a large volume of spent lithium-ion batteries (LIBs). The employment of harsh chemicals and lack of atom economy in the recycling method leads to significantly more environmental pollution and CO_2 emissions. Herein, Al foil wastes inherent in spent LIBs are used as the reducing agent and purifying agent in situ to induce the reduction of transition metal oxides and the targeted separation of impurity metals, and ultimately incorporated into the upcycled product at 100% atom efficiency.

emission reduction in the recycling of spent LIBs. It is necessary to develop green innovations that improve the reduction efficiency of Al foils while reducing the risk of hydrogen generation.

The key green chemistry principle of atom economy implies that all raw materials should be converted into the final product as much as possible (22). In previous in situ recycling, raw materials (current collectors) are employed as reducing agents and then separated in the form of hydroxide precipitation, but they do not enter the final products at all, so the final atom efficiency is 0%. Waste will still be generated after reuse, which not only does not reduce the amount of waste, but may actually make subsequent high-value utilization more difficult. For example, a unit mass of Al foils will generate 2.88 times as much $Al(OH)_3$ waste after reductive leaching. $Al(OH)_3$ exists in floc form with amorphous gel-like properties, which is difficult to be separated from the liquid. Therefore, based on the atom economy principle, using Al^0 as a functional reagent to enhance metal recovery and then entering the final electrode product may be a promising path for upcycling spent LIBs with the least economic and environmental costs.

In this work, the waste Al foils are fully exploited to its redox potential to replace multiple chemical reagents, and finally integrated into new $LiNi_{0.80}Co_{0.15}Al_{0.05}O_2$ (NCA) high-performance cathode materials. Firstly, mechanical activation pretreatment is employed to stimulate an in situ reduction reaction between the Cu/Al foils and spent cathode materials, followed by efficient CH_3COOH leaching without generating H_2 gas. Then, an Al foil-induced self-purification mechanism for targeted cation (Cu/Fe) precipitation in the liquid system has been developed to support the selective removal of Cu/Fe impurities. After all, Al foils enter the leaching solution as Al^{3+} ions, they are used as an aluminum source to prepare NCA precursor solution together with the Ni and Co elements. Based on a detailed life cycle assessment (LCA), we evaluated the new technology in terms of its environmental impact and economic benefits and found the new process to be highly beneficial. The mechanochemical upcycling of spent LCO batteries based on an atom economy strategy can be a model for the technological innovation of recycling other electronic wastes.

Results and Discussion

Mechanochemical Reduction: Lattice Evolution and Element Migration.

The phase analysis of ≤4 mm crushed product of spent LIBs is shown in Fig. 1A. It is a mixed powder composed of LCO, graphite, zero-valent Al and zero-valent Cu. The X-ray diffraction patterns of the mechanically activated products after different grinding times are shown in *SI Appendix*, Fig. S1. Although the characteristic peaks of graphite nearly disappear, the degree of attenuation of the main LCO electrode peak is small with increasing grinding time, which indicates that long-term low-speed ball milling at 400 rpm will not induce the lattice collapse of LCO. In contrast, the mechanochemical force from high-speed ball milling can cause the LCO lattice to change significantly, as shown in Fig. 1B. With increasing grinding speed, the peak intensity of LCO decreases rapidly, and the characteristic peaks of the Cu foils and Al foils nearly disappear. Specifically, the drifting of the (002) peak of LCO in Fig. 1C suggests that when ball milling exceeds 600 rpm, the mechanochemical force can destroy the order of the LCO lattice in the *c*-axis direction to the maximum extent, promoting the transformation of the crystal to the amorphous state. Fig. 1D shows that as the grinding speed is increased, the (111) peak of Al foils and the (111) peak of Cu foils attenuate significantly until they disappear. Additionally, the (200) peak of Al foils decreases and gradually merges with the (104) peak of LCO, which indicates that Al should react with LCO to form a mixed metal oxide. On the other hand, the surface morphology of the raw crushed products in Fig. 1E shows that LCO is a smooth-surfaced blocky particle. After mechanochemical activation, the diameter of LCO particles decreased greatly to ~2 μm, and fine scaly particles appeared on the surface, as shown in Fig. 1 *F–H*. The detailed micromorphology and element distribution of the mechanically activated products in Fig. 1 *I–L* show that the Cu and Al are uniformly distributed on the LCO particles. This indicates that LCO, Cu foils, and Al foils, which will not react spontaneously, undergo oxidation reaction under the induction of mechanochemistry. Since the face-centered cubic phases of Al and Cu disappear after the use of mechanical force, along with the Al and Cu being evenly distributed on the surface of the LCO final particles, it can be inferred that the Al^0 and Cu^0 lose electrons, convert into ionic states (Al^{3+}, $Cu^{1+/2+}$) and adsorb on the LCO particles. Therefore, it can be speculated that the LCO particles undergo a reduction reaction, resulting in the collapse of the layered structure.

Microsurface Analysis and Atomic-Level Evidence.

The valence state changes of zero-valent metals and high-valent transition metal elements in spent LIBs are direct evidence of mechanochemical interactions. Here, we focus on exploring the functional groups or valence components of metal elements within 5 nm of the surface before and after mechanical activation by XPS analysis. The Al 2p XPS spectra of the crushed materials are shown in Fig. 2 *A* and *B*, and the peak of Al_2O_3 appears at 75.1 eV (23). It is worth noting that due to the high activity of Al element, a dense oxide film tends to form on the surface of raw Al foils. However, the intensity of the Al_2O_3 peak increased five times after high-speed ball milling, which verified that a large amount of Al^{3+} ions were generated by mechanochemical action and adhered to the sample. The Cu 2p XPS spectra in Fig. 2 *C* and *D* give that Cu foils in the raw crushed materials are still mainly in the form of Cu^0 [located at 932.7 eV (24)], and a small amount of Cu^{2+} [located at 935.5 eV (25)] is also attached to its surface. The latter may be caused by hydrofluoric acid (HF) etching generated by electrolyte hydrolysis (26). More importantly, we detected 68.47% Cu^{2+} and 31.53% Cu^{1+} [located at 933.3 eV (27)] on the surface of the mechanochemical products, which verified the above conjecture ($Al^0 \rightarrow Al^{3+}$, $Cu^0 \rightarrow Cu^{1+,2+}$). The Co 2p XPS spectra in Fig. 2 *E* and *F* suggest that the content of high-valent Co^{3+} [located at 780.4 eV and 795.9 eV (28)] on the surface of the mechanochemical products decreased from 26.43 to 13.22%, down by about 50%, while the content of low-valent Co^{2+} [located at 781.8 eV and 797.3 eV (28)] increased from 73.57 to 86.78%.

The Co *K*-edge X-ray absorption near-edge structure (XANES) patterns of raw materials (Co-RM), mechanical activation products (Co-MA), and standard cobalt metal oxides are shown in Fig. 2G and *SI Appendix*, Fig. S2A. The absorption edges of Co-RM and Co-MA are located between the standard curves of CoO and Co_3O_4, which means that the average valence state of Co atoms is located between Co^{2+} and Co^{3+}, and there is no Co^0 at all before and after mechanochemical action. Further fitting analysis results of valence compositions of Co atoms, as shown in Fig. 2H and *SI Appendix*, Fig. S2B, indicate that the content of Co^{2+} in the cathode materials from spent LIBs after mechanical activation increased from 0.12 ± 0.05 to 0.72 ± 0.77, an increase of more than six times. It proves that the mechanochemical reaction after the introduction of zero-valent metals is a mild and well-controlled redox reaction. It does not directly reduce high-valent Co^{3+} to Co^0, but only converts a large amount of high-valent Co^{3+} into low-valent $Co^{(2+, 3+)}$. The Fourier transform of the Co R-edge EXAFS of Co-MA shows two strong peaks
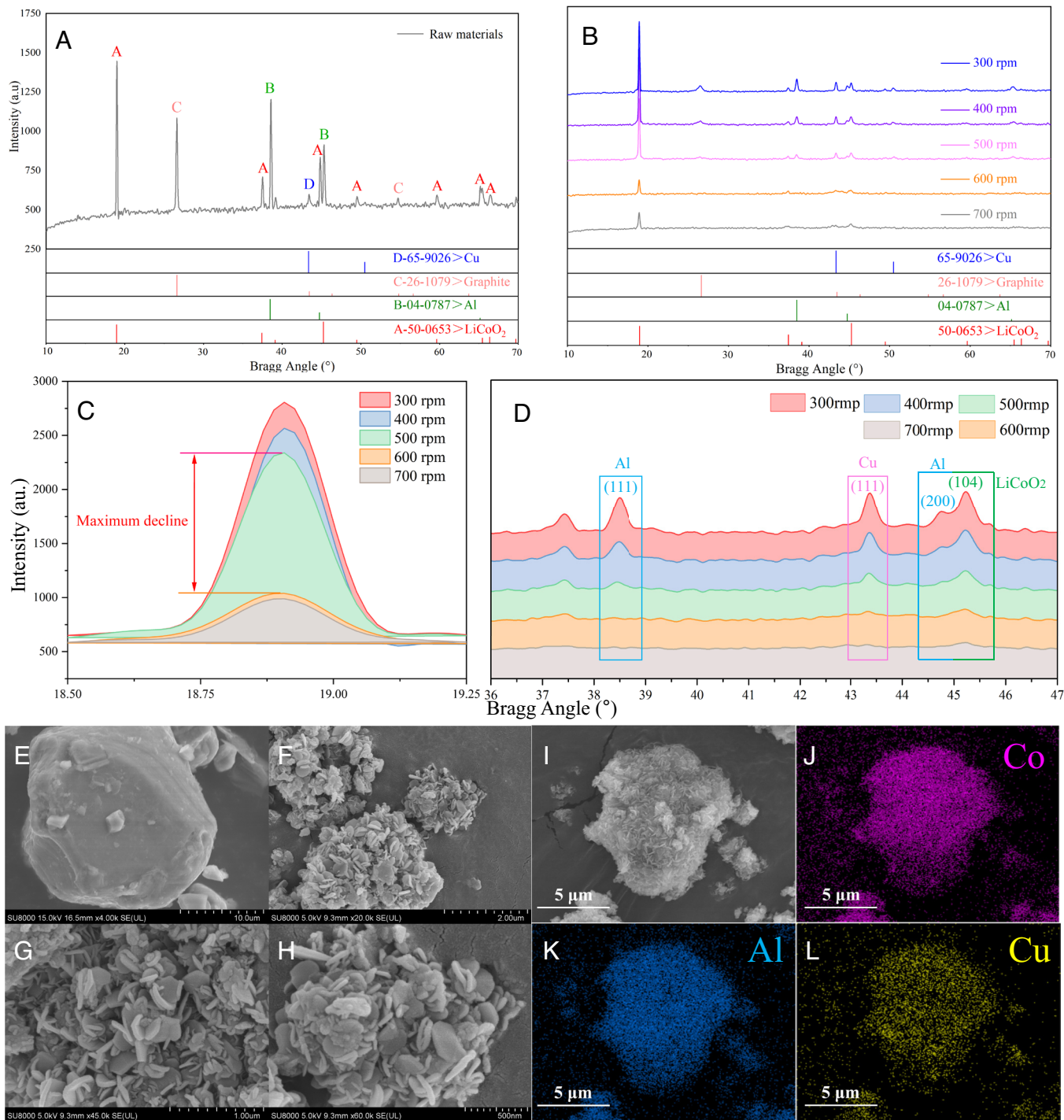
Fig. 1. Lattice evolution, element migration and chemical environment around atoms of spent LCO cathodes induced by mechanochemical action [(A) lattice evolution of raw crushed products; (B) lattice evolution process at different grinding speeds; (C) local magnification of (002) peak of LCO; (D) local magnification of the diffraction angle of 36°≤2θ≤47°; (E) surface morphology of raw crushed products; (F) surface morphology of the mechanochemical activation products; (G) and (H) are partial enlarged views of (F); (I–L) are surface morphology and element distribution of optimized grinding product].

around 1.75 Å and 2.25 Å in Fig. 2*I*, which are mainly attributed to Co-O and Co-Co coordination (29, 30). It should be noted that the two consecutive peaks at 3 Å correspond to the Co-Co signals with different spacings in LiCoO$_2$. Through the least-square analysis and quantification of extended X-ray absorption fine structure (EXAFS) fitting curve, as shown in Fig. 2*J*, we determined the chemical bond lengths of the cobalt atomic centers and their coordination numbers of the raw materials and mechanical activation products in *SI Appendix*, Table S1. As the valence of cobalt decreases, the bond length of Co-O increases, while the

bond length of Co-Co decreases. After the mechanochemical action, the bond length of Co-O in the waste cathode materials increases from 1.90 ± 0.01 Å to 1.94 ± 0.02 Å, and the coordination number increased from 3.0 ± 0.6 to 3.2 ± 1.0; the bond length of Co-Co decreases from 2.80 ± 0.02 Å to 2.43 ± 0.04 Å, and the coordination number increases greatly from 3.2 ± 0.9 to 7.0 ± 0.2. All these prove that the mechanochemical reaction induces the efficient reduction of waste cathode materials, and the low-valence cobalt increase significantly. Furthermore, the growth of chemical bonds of Co-O verifies the occurrence of
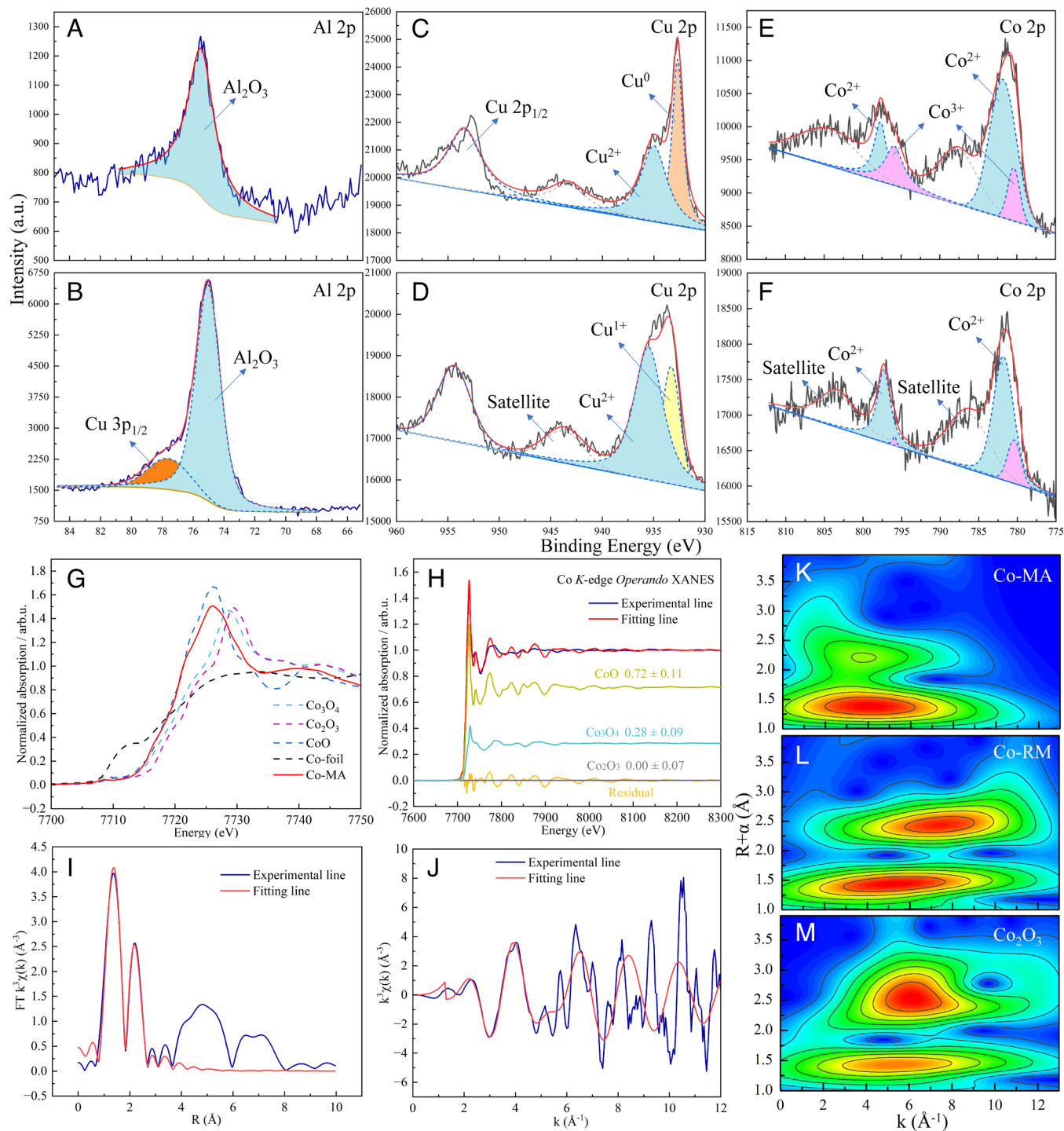
Fig. 2. Microsurface functional group and chemical environment around atoms of spent LCO cathodes induced by mechanochemical action [(*A–F*) XPS spectrum of Al 2p, Cu 2p and Co 2p, where *A*, *C*, and *E* are raw materials and *B*, *D*, and *F* are mechanochemical products; (*G*) Co *K*-edge XANES of Co foils, Co-RM, Co-MA; (*H*) valence fitting analysis of Co atoms in Co-MA; (*I*) fourier transform of EXAFS spectrum in R space and the best fitting result for Co-MA; (*J*) fourier transform of EXAFS spectrum in K space and the best fitting result for Co-MA; (*K–M*) WT for the k³-weighted EXAFS signals of Co-MA, Co-RM and Co₂O₃].

lattice collapse and cell distortion in spent LCO cathodes, and the large increase in the coordination number also implies the transformation of the LCO cell from an ordered arrangement to an amorphous state, which all show a surge in the internal energy of the sample after the mechanochemical reaction. These deductions can be confirmed by the wavelet transform, as shown in Fig. 2 *K–M* and *SI Appendix,* Fig. S3. The Co K-edge contour plots of Co-RM show two maximum intensities, and their positions are consistent with Co₂O₃ scattering, while Co-MA only

shows one intensity maximum, and its position is between Co foil and CoO. Only an increase in the internal energy can induce such an irregular directional shift in the local coordination environment of Co centers. In summary, the enhanced mechanochemical action by introducing zero-valent metals promotes the controllable redox reaction of waste cathode materials, and meanwhile, a large amount of internal energy [i.e., Wigner energy (31)] is stored inside, causing its crystal structure to collapse, which will effectively promote the subsequent leaching.

Verification and Optimization of Leaching Effect of In Situ Reduction. The stored internal energy from ball-milling promotes dissolution. We use acetic acid (CH_3COOH) to verify the leaching effect of weak organic acid on the different samples, as shown in *SI Appendix,* Fig. S4*A*. The direct leaching of 2 mol/L CH_3COOH of the ≤4 mm crushed products from spent LIBs shows that only 57.17% Li and 33.4% Co are dissolved into the liquid phase, and the leaching rates of Cu and Al are 17.96% and 50.22%, respectively. After the addition of 6 vol.% H_2O_2, the leaching rates of Li and Co increase to 100% and 73.21%, respectively, while that of Al decreases to 15.14%. Nevertheless, CH_3COOH leaching of the mechanical activated products results in the leaching rates of Li and Co reaching 92.37% and 92.51%, respectively, while the leaching rates of Cu and Al also increase significantly to 67.51% and 65.43%. Since it does not introduce impurity ions, H_2O_2 is recognized as one of the best reducing agents and its redox reactions with $LiCoO_2$ at pH ~1 are shown below (32):

$$H_2O_2 = O_2(gas) + 2H^+ + 2e^- \qquad [1]$$

$$LiCoO_2 + 4H^+ + e^- = Li^+ + Co^{2+} + 2H_2O \qquad [2]$$
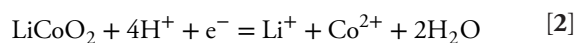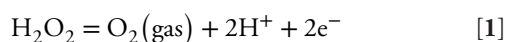
However, the thermal stability of H_2O_2 is poor, and the reaction rate of reaction (1) is significantly higher than that of reaction (2), resulting in excessive consumption of H_2O_2. Under mechanochemically enhanced leaching, the waste cathode materials undergoes a direct redox reaction with Al foils and Cu foils as follows:

$$3LiCoO_2 + Al + 12H^+ = 3Li^+ + 3Co^{2+} + Al^{3+} + 6H_2O \quad [3]$$

$$2LiCoO_2 + Cu + 8H^+ = 2Li^+ + 2Co^{2+} + Cu^{2+} + 4H_2O \quad [4]$$
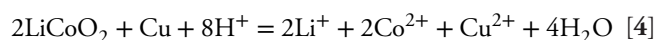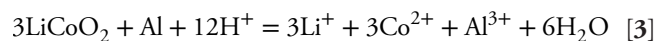
During the mechanochemical process, the Al foils and Cu foils, which are originally insoluble in weak acetic acid, lose their electrons to form soluble Al^{3+} and Cu^{2+}, while the acid-insoluble Co^{3+} in LCO is reduced to soluble Co^{2+} by obligatory absorption of electrons. This charge rebalancing simultaneously enhances the leaching of Li, Co, Al, and Cu in weak acids. In addition, *SI Appendix,* Fig. S4 *B–D* shows the optimization of the leaching conditions of the 600 rpm-activated products. With a liquid-to-solid ratio of 100 mL/g, an acetic acid concentration of 2 mol/L and a reaction temperature of 60 °C, the leaching rates of Li, Co, Al and Cu in the ≤4 mm crushed products are close to 100%. Therefore, the mechanical activation pretreatment can promote the charge neutralization of insoluble metals in the crushed products and realize the in situ reduction in the spent LCO cathode. Synchronous leaching of multiple metals is thus achieved.

Self-Purification by ORP-Control via the Inherent Al Foils in the Leaching Liquid System. In conventional hydrometallurgical recovery, differences in the solubility product constants (K_{sp}) can be used to achieve the removal of metal impurity precipitates; for instance, Fe, Al, and Cu ions can be separated from Ni, Co, and Mn ions by adjusting the temperature, pH, and initial concentration. We consider Cu cation as a typical impurity and use the *E*-pH Pourbaix diagram of Cu-Co-H_2O system to simulate the evolution of the Cu-ion phase boundary during the pH adjustment process, as shown in Fig. 3*A*. When the pH of the solution is adjusted from 3.0 to 6.5, the concentration of Cu ions decreases from 1 mol/L

to 1 × 10^{-6} mol/L, demonstrating the removal of soluble Cu ions; however, the theoretical removal boundary of Cu ions coincides with the precipitation boundary of Co ions, which is the initial concentration of Co-ion precipitates. Therefore, adjusting the pH is likely to cause the coprecipitation of Cu and Co ions, which would result in the loss of precious Co ions needed to prepare NCA precursor. Temperature is also an important parameter in the conventional separation method. The *E*-pH phase diagrams of typical metal impurity ions at different temperatures are shown in *SI Appendix,* Fig. S5. The precipitation boundary lines of the Cu and Al ions shift in the direction of decreasing pH with increasing temperature; however, the difference in pH between the two fluctuates by only 0.6, which also makes it difficult to realize the complete separation of the Al and Cu ions.

CH_3COOH is used as the leaching agent, and the pH of the leaching solution fluctuates between 2.0 and 4.0. Thus, the phase distribution of impurity ions in the liquid system is shown in the orange background area in Fig. 3*B*. The oxidation/reduction potential (ORP) *E*, which is the *y*-axis of the Pourbaix diagram, gives us a systematic handle to separate out Cu cation impurities from the Li/Co in the aqueous solution. The ORP corresponds to effective O_2(gas) and H_2(gas) partial pressures inside the water (ORP↑ pO_2↑ pH_2↓), and zero-valent Al, being highly reactive with pO_2 once its oxide passivation layer is removed by the acid, can greatly reduce the ORP of the aqueous solution. When the solution pH = 2.0 to 4.0, the electrode potential for the conversion of Cu^{2+} to Cu is approximately 0.4 V, while the electrode potential for the conversion of H^+ to H_2 is 0 to 0.2 V; thus, the potential of Cu ions is always higher than that of H ions. Moreover, the potentials of the Co ions will not exceed that of the H ions until the solution pH is >5. Therefore, when Al foils are added to the CH_3COOH leaching solution, Cu^{2+} will preferentially absorb electrons and cross the curve corresponding to the reduction reaction and enter the zero-valent Cu phase region; thus, the directional precipitation of Cu is realized, while H^+, Li^+ and Co^{2+} still exist in the liquid phase, as shown in Fig. 3*C*. More importantly, the precipitated zero-valent Cu will not redissolve into the dilute acid solution, avoiding secondary pollution problems. To test the actual effect of the targeted purification mechanism, we conducted verification experiments on leaching solution systems, as shown in Fig. 3*D*. The Cu ion residue in the solution after the targeted precipitation tends to be near zero, and the loss of precious metal ions can be almost ignored; these results prove the success of the self-purification strategy. Notably, the pH at which Fe^{3+} begins to precipitate in the solution is 1.149, and when the solution pH reaches 2.813, Fe^{3+} can be completely precipitated; thus, the solution pH range is limited by the CH_3COOH leachate, and the ORP influenced by the added larger Al foils not only removes soluble Cu ions but also thoroughly remove the Fe ions from the solution (33). Actual ion concentration in different batches of self-purification residual liquid has been shown in *SI Appendix,* Table S2, which demonstrates the feasibility of the synergistic removal of copper and iron impurity ions. Therefore, the self-purification of the Cu and Fe ions in the leaching solution can be effectively realized by reusing the large Al foils pieces from the crushed products of spent LIBs.

Crystal Structure and Electrochemical Properties of the Regenerated High Nickel Lithium-Ion Batteries. The Al^{3+} ions in the self-purified leachate are no longer removed, but instead further used directly as an Al source for the preparation of cathode materials; thus, Al self-supply method is realized. The morphology and elemental distribution of the precursor and the regenerated cathode materials are shown in *SI Appendix,* Figs. S6
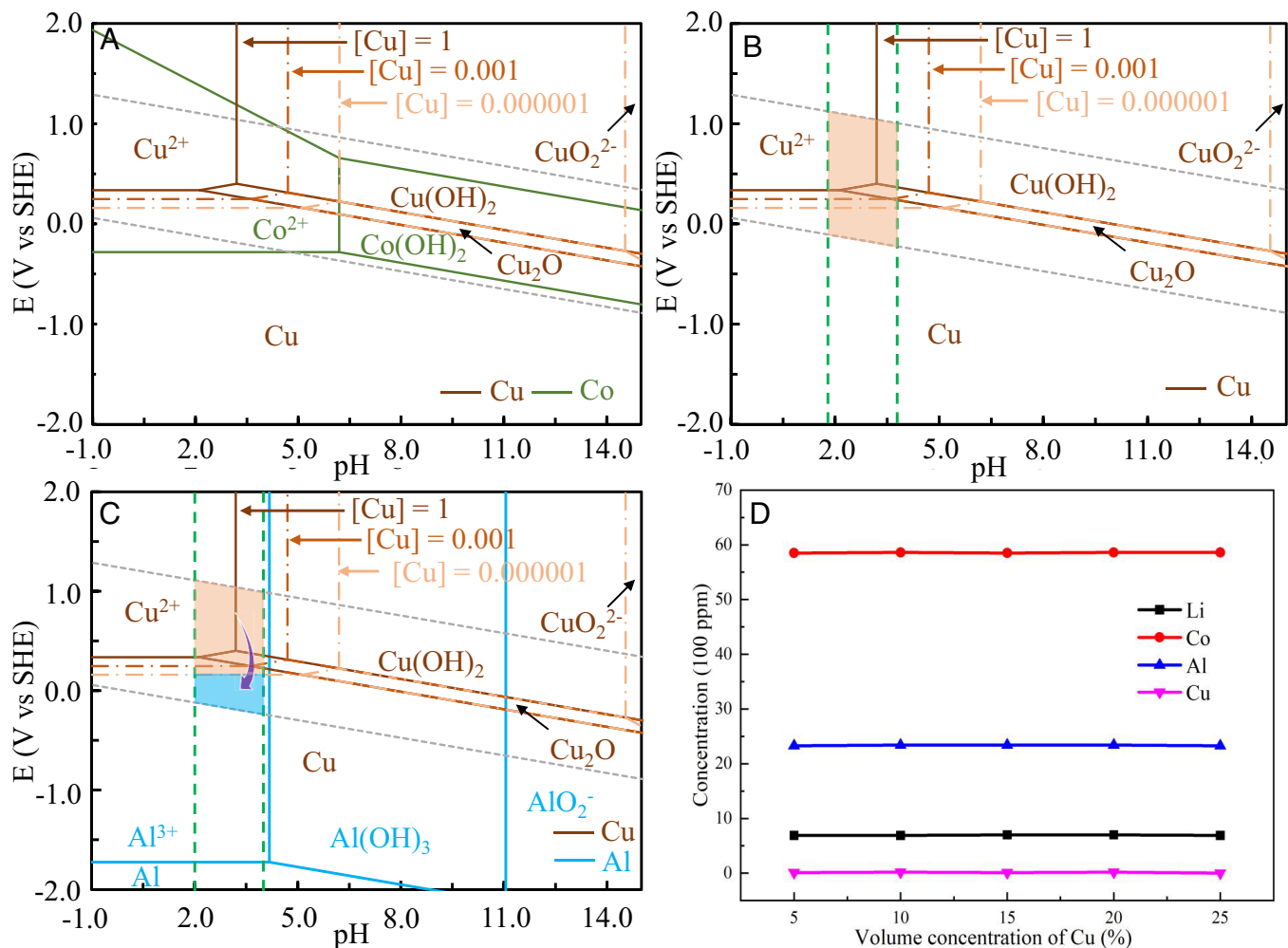
Fig. 3. Mechanism and effect of self-purification based on E-pH diagrams [(A) E-pH diagram of Co and Cu with different concentrations; (B) phase migration of Cu with different concentrations; (C) mechanism of Al^0-induced directional transfer of Cu ions; (D) selective purification effect of Cu ions in solution].

and S7, all exhibiting similar particle size, plump shape and uniform elemental distribution. To check the crystalline state of the regenerated $LiNi_{0.80}Co_{0.15}Al_{0.05}O_2$ (NCA) cathode, we used GSAS software with the EXPGUI program to refine the structure of its X-ray diffraction (XRD) pattern (34); the results are shown in *SI Appendix*, Table S3 and Fig. 4A. According to the Rietveld refinement, the fitting parameters (R_{wp} and R_{exp}) of the differential peaks are 2.84% and 1.69%, respectively, and χ^2 is 3.93, which indicates that the lattice structure of the regenerated NCA cathode is very close to the theoretical crystalline state. The Rietveld refinement results show that the regenerated NCA cathode has a perfect layered structure, 100% belonging to the R3M space group, and does not contain nonlamellar oxide phase such as NiO. The reference value (c/a) of the ideal densely stacked hexagonal-laminated lattice is 4.899, while the c/a value of the regenerated NCA cathode is 4.937, which shows good stability of the layered structure (35). The spatial parameter I_{003} / I_{104}>1.2 means a lower degree of cation mixing, while the I_{003} / I_{104} of the regenerated NCA cathode is 2.412, which indicates that the cations in the crystal structure are in a highly ordered arrangement (36, 37). Further fitting results also show that only 0.916% of the divalent Ni ions occupy the position of the Li ions in the $LiNiO_2$ phase, which is lower than 1.5% in similar literature (38). The actual electrochemical cycling performance of the regenerated NCA cathode and commercial NCA materials are shown in Fig. 4 *B–E* and *SI Appendix*, Fig. S8, respectively. The

results suggest that the charge transfer resistance of our regenerated NCA cathode at room temperature is 229 Ω, which is higher than that of commercial NCA materials. The rate performance of the regenerated NCA cathode at different charge and discharge rates are as follows: 211.78 mAh/g at 0.1C, 190.08 mAh/g at 0.2C, 184.92 mAh/g at 0.3C, 177.69 mAh/g at 0.4C, 170.45 mAh/g at 0.5C, and 155.99 mAh/g at 1C. The first discharge capacity of the regenerated NCA cathode is 215.28 mAh/g, and the capacity retention rate after 180 cycles is approximately 80%; in contrast, the first discharge capacity of commercial NCA materials is 194.56 mAh/g, and their capacity retention rate after 180 cycles is approximately 75% under similar physicochemical conditions. The NCA cathode materials prepared by the direct upcycling of spent LIBs exhibit excellent crystallinity and a low degree of cation mixing; thus, their electrochemical cycling performance is up to or even slightly better than that of commercial products.

Technoeconomic Analysis and Environmental Impact Assessment. In this study, the coupling of materials flow and life cycle cost analysis is used to complete the technoeconomic analysis of the mechanochemical upcycling method. The economic values and quantitative parameters of each step are given in the *SI Appendix*, and the results of technoeconomic analysis are shown in Fig. 5A. The price of waste raw materials is quoted from China National Resources Recycling Association, the prices of chemical additives and recycling products are from the industry quotation
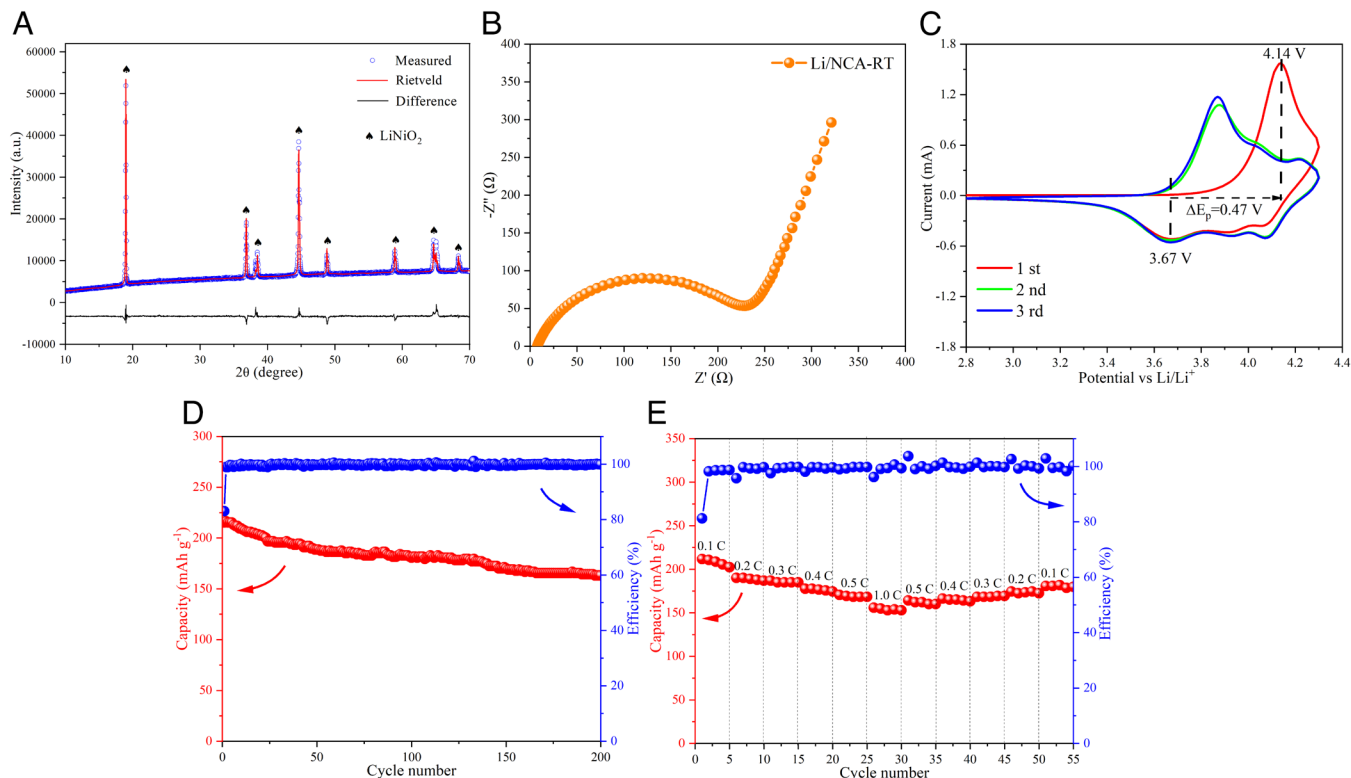
Fig. 4. Lattice analysis and electrochemical performance of newborn NCA cathodes prepared from spent LCO batteries (*A* is structural refinement analysis of NCA cathode materials; *B* is electrochemical impedance spectroscopy; *C* is cyclic voltammetry curve; *D* is battery cycle performance at 0.2 C; *E* is battery rate performance).

of Shanghai Nonferrous Metals Network on Sep. 9, 2022, and the prices of industrial water and industrial electricity are Chinese average price over the same period. The technoeconomic analysis shows that the total cost of raw materials for spent LIBs, and their disposal process is 3644.37 CNY per kilogram, the sales revenue of the recycling product is 4300.68 CNY per kilogram, and the comprehensive profit rate reaches 18%. The coprecipitation step is the most intensive step of chemical additives, and the cost of the corresponding chemical additives is 1590.86 CNY, accounting for about 43.65% of the total input. Due to shipping obstacles and ore supply difficulties caused by the COVID-19 pandemic, lithium carbonate is the most expensive additive, and its procurement cost accounts for about 52.42% of the total input. Since NCA batteries have been used as key components in advanced electric vehicles such as Tesla Model S, 3, X and Y, the regenerated NCA cathode products are a main source of economic income, and its economic benefit accounts for about 98.95% of the total output.

The environmental impact comparison between our new green upcycling process and the conventional hydrometallurgical process for recycling spent LIBs is analyzed by the life cycle assessment (LCA) method, and data lists are shown in the *SI Appendix*. The LCA results of greenhouse gas emissions, water acidification, and water eutrophication in Fig. 5*B* and *SI Appendix*, Fig. S9 show that acid leaching and coprecipitation are the main steps that increase the environmental impact. In the conventional acid leaching step, to neutralize the alkaline leaching residue, a large amount of strong inorganic acid (e.g., H_2SO_4) is consumed, and an additional reducing agent is necessary, which increases the environmental footprint. Thus, all environmental impact indicators of conventional technologies are higher than those of the new technology. In the coprecipitation step, the new technology is supplemented with appropriate amounts of $(CH_3COO)_2Ni$ and $(CH_3COO)_2Co$.

Although the environmental impact of the preparation process of these organic additives is higher than that of inorganic additives, acetate waste has high vapor pressure; thus, it is easy to volatilize and recover, resulting in a smaller environmental impact. As a consequence, the new technology has lower global warming potential, acidification potential and eutrophication potential than the traditional technology, with decreases of 45.83%, 9.16%, and 15.02%, respectively. Fig. 5*C* shows that the new technology is far lower than the traditional technology in terms of human toxicity potential, and the final potential value drops by 95.09%. This reason is that due to the high hole-blocking rate in the deep sieve-screening process in the traditional technology, a large amount of cobalt is not effectively recovered, causing them to be abandoned in the ecosystem, resulting in significant heavy metal pollution. In contrast, the new technology adopts moderate sieve-screening, and the recovery rate of the cathode materials increased to more than 98%. This in situ green upcycling therefore illustrates how one can significantly reduce environmental pollution and greenhouse gas emissions while supporting profitability of LIBs recycling industry and other circular economy industries.

Conclusion

In this work, we use the mechano-chemical upcycling of spent $LiCoO_2$ to new $LiNi_{0.80}Co_{0.15}Al_{0.05}O_2$ battery to illustrate the unique advantages of atom economy strategy. All components in the waste should be reasonably disposed of and enter the recycling products as much as possible. In contrast to waste reuse concept in the past, waste Al foils are used as a supply source for the regenerated NCA cathode materials after being employed as substitute reducing agents and purifying agents. Despite the lower consumption of chemical additives, the metal recovery rate from spent LIBs still
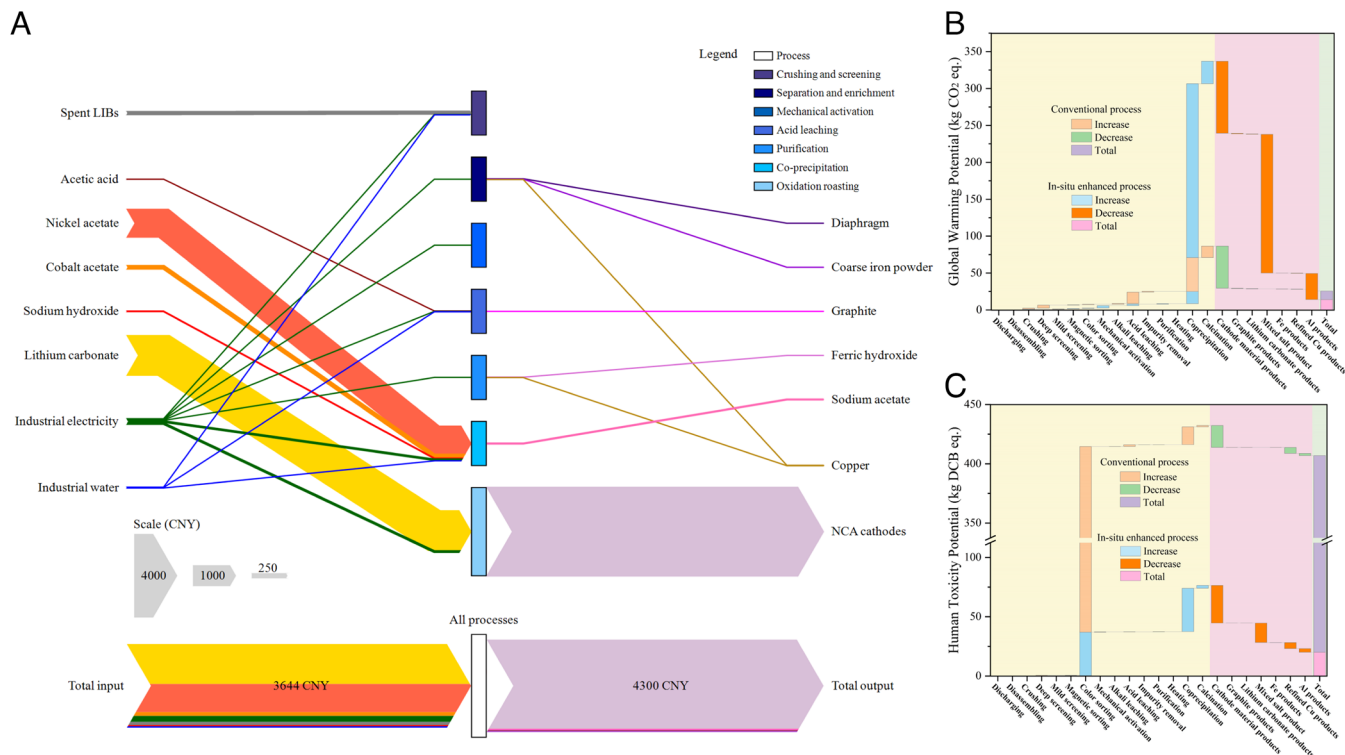
Fig. 5. Technoeconomic analysis and environmental impact assessment of mechanochemical upcycling process for spent lithium-ion batteries [(*A*) technoeconomic analysis; (*B*) global warming potential assessment; (*C*) human toxicity potential assessment].

reaches nearly 100%, and the electrochemical performance of the regenerated NCA cathode materials has reached the commercial application standard. More beneficially, compared with the conventional recycling process of spent LIBs, the carbon emission, acidification potential, and eutrophication potential of this new technology decrease by 45.83%, 9.16%, and 15.02%, respectively, while the human toxicity potential drops greatly by 95.09%. Such a direct upcycling paradigm can be useful in a broader field of waste management and carbon neutralization, and assist the decarbonization and sustainable development of new industries in the emergent global energy transition. As a final note, the pollution of organic volatiles is another difficult problem that hinders the industrial-scale recovery of spent LIBs. We believe that the mechanochemical reaction process will also promote the degradation of long-chain alkanes, and it will be parsed in detail in another work.

Materials and Methods

Raw Materials and Reagents. The spent LCO batteries of the year-2015 model Motorola mobile phones were dismantled and used as experimental materials. The reagents used in the experiments were analytically pure and purchased from the unified reagent management platform of Tsinghua University. The experimental water was deionized water that was uniformly prepared by the School of Environment, Tsinghua University. It should be noted here that this study demonstrates the whole process of preparing NCA batteries from spent LCO batteries. Since ternary LIBs have similar crystal structure and material composition to LCO batteries, this method can theoretically be extended to the preparation of spent ternary LIBs into $LiNi_xCo_yMn_zAl_mO_2$ batteries.

Mechanochemical Upcycling Process of Spent LCO Batteries. The data quality flow chart of the green upcycling of spent LCO batteries is shown in *SI Appendix*, Fig. S10. First of all, all spent LIBs need to be fully discharged in a 5% NaCl solution for 24 h to induce the lithium ions in the graphite anode to return to the cathode materials (39). After complete crushing and screening, undersized products with particle sizes of less than 4 mm (≤4 mm crushed products)

oversized products with particle sizes of greater than 4 mm (≥4 mm crushed products) were obtained, accounting for 75.44 wt.% and 24.56 wt.% of the total mass, respectively. This sieve aperture can ensure that the materials under the sieve undergo sufficient redox reaction (33). The ≥4 mm crushed products were sorted in sequence by a pulsating airflow to recover the plastic diaphragm, magnetic separation to recover the steel flakes, color separation to recover the Cu foils, until finally, a small amount of larger-sized Al foil fragments were obtained (40). After mechanical activation, ≤4 mm crushed products were leached with acetic acid and filtered to obtain a leaching solution and graphite residue. On the other hand, the large Al foils obtained from the ≥4 mm crushed products were thrown into the CH_3COOH leachate to precipitate and separate the copper sludge and a small amount of iron sludge, in order to obtain a purified leaching solution.

Preparation of New Ternary Cathode Materials from Purified Leachate. Firstly, the purified leachate needs to be characterized for its specific elemental concentrations to calculate the subsequent additions of lithium, nickel, and cobalt. Next, the purified leachate should be stirred uniformly at 500 to 600 rpm at moderate concentration and temperature, while coprecipitation and aging are performed after slow dropwise addition of diluted nickel acetate, cobalt acetate, or sodium meta-aluminate according to the molar ratio of Ni: Co: Al = 16:3:1. Under low-speed grinding and stirring, the NCA precursor obtained from coprecipitation should be thoroughly mixed with lithium carbonate at a molar ratio of 1:1.05. Finally, the NCA precursor mixtures can be sent to a high-temperature furnace for roasting and crystallization in a liquid oxygen environment to achieve the regenerated NCA cathode materials. The oxygen-rich calcination process requires a slow ramp-up to 800 °C at 5 °C/min, holding for 24 h, followed by a slow ramp-down at 5 °C/min. Excessive temperature fluctuations and insufficient oxygen content are prone to result in the failure of the NCA cathode.

Electrochemical Performance Test. First, the NCA cathode materials, carbon black, and polyvinylidene fluoride were evenly mixed at a mass ratio of 8:1:1 and stirred evenly with N-methylpyrrolidone as the solvent. Next, the fresh slurry was evenly coated on an Al foil, dried in a vacuum drying oven at 70 °C for 12 h, and punched into a circular disk with a diameter of 8 mm to obtain a serviceable cathode. The assembly of the battery was carried out in a glove box filled with argon gas. Finally, the CR2032 button cell was assembled with the above cathode,

lithium metal (anode electrode), a Celgard 2,400 microporous polypropylene film (separator), and 6 μL of electrolyte composed of 1.0 mol/L $LiPF_6$ in EC:DEC:EMC = 1:1:1 for electrochemical performance testing. The mass loading of NCA cathode materials is 1.7 mg/cm^2.

Material Characterization and Analytical Calculations. The analytical instruments used in this research were provided by the testing platform at Tsinghua University, and all instruments had obtained China metrology accreditation. Under the test conditions of a copper target at 40 kV and 30 mA, X-ray diffraction (XRD, Philips PW 1700, USA) was employed to characterize the crystal structures of different samples. Field-emission scanning electron microscopy equipped with energy dispersive spectroscopy (Carl Zeiss MERLIN Compact, Germany) was performed to capture the surface morphology and the elemental distribution, respectively. Synchrotron X-ray absorption near-edge structure (XANES) spectroscopy was supported by Shanghai Light Source. Inductively coupled plasma optical emission spectrometry (ICP-OES, PerkinElmer, OPTIMA 2000, USA) was used to analyze the concentration of metal ions in the leaching solution. Based on Gibbs free energy, Faraday's law and Nernst equation, E-pH Pourbaix diagram can be obtained for phase transfer predictions (41, 42). The calculation methods and process parameters of E-pH curve has been shown in *SI Appendix*. On the

other hand, the data list and soft parameters of life cycle assessment method and technoeconomic analysis have also been shown in *SI Appendix*.

Data, Materials, and Software Availability. All study data are included in the article and/or *SI Appendix*.

1. G. Harper *et al.*, Recycling lithium-ion batteries from electric vehicles. *Nature* **575**, 75–86 (2019).
2. D. Castelvecchi, Electric cars: The battery challenge. *Nature* **596**, 336–339 (2021).
3. M. Jiao *et al.*, Recycling spent $LiNi_{1-x-y}Mn_xCo_yO_2$ cathodes to bifunctional NiMnCo catalysts for zinc-air batteries. *Proc. Natl. Acad. Sci. U.S.A.* **119**, e2202202119 (2022).
4. X. Lu *et al.*, A solid-state electrolysis process for upcycling aluminium scrap. *Nature* **606**, 511–515 (2022).
5. C. Stinn, A. Allanore, Selective sulfidation of metal compounds. *Nature* **602**, 78–83 (2022).
6. J. Baars, T. Domenech, R. Bleischwitz, H. E. Melin, O. Heidrich, Circular economy strategies for electric vehicle batteries reduce reliance on raw materials. *Nat. Sustain.* **4**, 71–79 (2021).
7. E. A. Olivetti, G. Ceder, G. G. Gaustad, X. K. Fu, Lithium-ion battery supply chain considerations: Analysis of potential bottlenecks in critical metals. *Joule* **1**, 229–243 (2017).
8. X. T. Ma *et al.*, Recycled cathode materials enabled superior performance for lithium-ion batteries. *Joule* **5**, 2955–2970 (2021).
9. M. Y. Chen *et al.*, Recycling end-of-life electric vehicle lithium-ion batteries. *Joule* **3**, 2622–2646 (2019).
10. M. K. Tran, M. T. F. Rodrigues, K. Kato, G. Babu, P. M. Ajayan, Deep eutectic solvents for cathode recycling of Li-ion batteries. *Nat. Energy* **4**, 339–345 (2019).
11. E. S. Fan *et al.*, Sustainable recycling technology for Li-ion batteries and beyond: Challenges and future prospects. *Chem. Rev.* **120**, 7020–7063 (2020).
12. K. Kim *et al.*, Electrochemical approaches for selective recovery of critical elements in hydrometallurgical processes of complex feedstocks. *iScience* **24**, 102374 (2021).
13. G. W. Zhang *et al.*, Recycling of valuable metals from spent cathode material by organic pyrolysis combined with in-situ thermal reduction. *J. Hazard. Mater.* **430**, 128374 (2022).
14. Z. Huang, R. J. Qiu, K. Y. Lin, J. J. Ruan, Z. M. Xu, In situ recombination of elements in spent lithium-ion batteries to recover high-value gamma-$LiAlO_2$ and $LiAl_5O_8$. *Environ. Sci. Technol.* **55**, 7643–7653 (2021).
15. K. Kim, D. Raymond, R. Candeago, X. Su, Selective cobalt and nickel electrodeposition for lithium-ion battery recycling through integrated electrolyte and interface control. *Nat. Commun.* **12**, 6554 (2021).
16. N. Peeters, K. Binnemans, S. Riano, Recovery of cobalt from lithium-ion battery cathode material by combining solvoleaching and solvent extraction. *Green Chem.* **24**, 2839–2852 (2022).
17. W. Q. Wang, Y. C. Zhang, X. G. Liu, S. M. Xu, A simplified process for recovery of Li and Co from spent $LiCoO_2$ cathode using Al foil as the in situ reductant. *ACS Sustain. Chem. Eng.* **7**, 12222–12230 (2019).
18. M. Joulie, E. Billy, R. Laucournet, D. Meyer, Current collectors as reducing agent to dissolve active materials of positive electrodes from Li-ion battery wastes. *Hydrometallurgy* **169**, 426–432 (2017).
19. C. Peng, F. P. Liu, A. T. Aji, B. P. Wilson, M. Lundstrom, Extraction of Li and Co from industrially produced Li-ion battery waste–Using the reductive power of waste itself. *Waste Manage.* **95**, 604–611 (2019).
20. A. Chernyaev *et al.*, The efficiency of scrap Cu and Al current collector materials as reductants in LIB waste leaching. *Hydrometallurgy* **203**, 105608 (2021).
21. Y. Jia *et al.*, Life cycle assessment of hydrogen peroxide produced from mainstream hydrogen sources in China. *J. Clean. Product.* **352**, 131655 (2022).
22. B. M. Trost, The atom economy–a search for synthetic efficiency. *Science* **254**, 1471–1477 (1991).
23. X. T. Gao, I. E. Wachs, Structural characteristics and reactivity properties of highly dispersed Al_2O_3/SiO_2 and V_2O_5/Al_2O_3/SiO_2 catalysts. *J. Catal.* **192**, 18–28 (2000).
24. I. Dontas, S. Ladas, S. Kennou, Study of the early stages of Cu/6H-SiC(000–1) interface formation. *Diam. Relat. Mater.* **12**, 1209–1212 (2003).
25. Y. Sun *et al.*, Revealing the active species of Cu-based catalysts for heterogeneous Fenton reaction. *Appl. Catal. B: Environ.* **258**, 117985 (2019).
26. X. L. Zeng, J. H. Li, L. L. Liu, Solving spent lithium-ion battery problems in China: Opportunities and challenges. *Renew. Sust. Energ. Rev.* **52**, 1759–1767 (2015).
27. J. L. Gong *et al.*, Synthesis of ethanol via syngas on Cu/SiO_2 catalysts with balanced Cu^0-Cu^+ Sites. *J. Am. Chem. Soc.* **134**, 13922–13925 (2012).
28. J. D. Yu *et al.*, In-situ enhanced catalytic reforming behavior of cobalt-based materials with inherent zero-valent aluminum in spent lithium ion batteries. *Appl. Catal. B: Environ.* **303**, 120920 (2022).
29. J. K. Wang *et al.*, CoO/CoP heterostructured nanosheets with an O-P interpenetrated interface as a bifunctional electrocatalyst for Na-O_2 battery. *ACS Catal.* **8**, 8953–8960 (2018).
30. T. T. Sun *et al.*, Single-atomic cobalt sites embedded in hierarchically ordered porous nitrogen-doped carbon as a superior bifunctional electrocatalyst. *Proc. Natl. Acad. Sci. U.S.A.* **115**, 12692–12697 (2018).
31. C. A. Hirst *et al.*, Revealing hidden defects through stored energy measurements of radiation damage. *Sci. Adv.* **8**, 2733 (2022).
32. Z. Y. Lu *et al.*, High-efficiency oxygen reduction to hydrogen peroxide catalysed by oxidized carbon materials. *Nat. Catal.* **1**, 156–162 (2018).
33. J. D. Yu, Q. Y. Tan, J. H. Li, Exploring a green route for recycling spent lithium-ion batteries: Revealing and solving deep screening problem. *J. Clean. Product.* **255**, 120269 (2020).
34. J. Wu, A. Mackenzie, N. Sharma, Recycling lithium-ion batteries: Adding value with multiple lives. *Green Chem.* **22**, 2244–2254 (2020).
35. Y. N. Zhang *et al.*, Novel efficient regeneration of high-performance $Li_{1.2}[Mn_{0.56}Ni_{0.16}Co_{0.08}]O_2$ cathode materials from spent $LiMn_2O_4$ batteries. *J. Alloy Compd.* **783**, 357–362 (2019).
36. H. Ronduda *et al.*, On the sensitivity of the Ni-rich layered cathode materials for Li-ion batteries to the different calcination conditions. *Nanomaterials* **10**, 2018 (2020).
37. M. J. Zhu *et al.*, Preparation and electrochemical properties of $LiNi_{2/3}Co_{1/6}Mn_{1/6}O_2$ cathode material for lithium-ion batteries. *Materials* **14**, 1766 (2021).
38. Y. J. Zhang *et al.*, Synthesis of high performance nano-over-lithiated oxide coated $LiNi_{0.6}Co_{0.2}Mn_{0.2}O_2$ from spent lithium ion batteries. *Mater. Res. Express* **6**, 085521 (2019).
39. J. P. Pender *et al.*, Electrode degradation in lithium-ion batteries. *ACS Nano* **14**, 1243–1295 (2020).
40. X. H. Zhong *et al.*, Pyrolysis and physical separation for the recovery of spent $LiFePO_4$ batteries. *Waste Manage.* **89**, 83–93 (2019).
41. C. R. Yang, F. Jiao, W. Q. Qin, Cu-state evolution during leaching of bornite at 50°C. *T. Nonferr. Metal. Soc.* **28**, 1632–1639 (2018).
42. Y. K. Li *et al.*, Recycling of spent lithium-ion batteries in view of green chemistry. *Green Chem.* **23**, 6139–6171 (2021).

Supporting Information

Mechano-chemical upcycling of spent $LiCoO_2$ to new $LiNi_{0.80}Co_{0.15}Al_{0.05}O_2$ battery: an atom economy strategy

Jiadong Yu[a], Ju Li[b], Shang Zhang[a], Fan Wei[a], Yanjun Liu[a], Jinhui Li[a] *

[a]State Key Joint Laboratory of Environment Simulation and Pollution Control, School of Environment, Tsinghua University, Beijing 100084, China

[b]Department of Nuclear Science and Engineering and Department of Materials Science and Engineering, Massachusetts Institute of Technology, Cambridge, MA 02139, USA
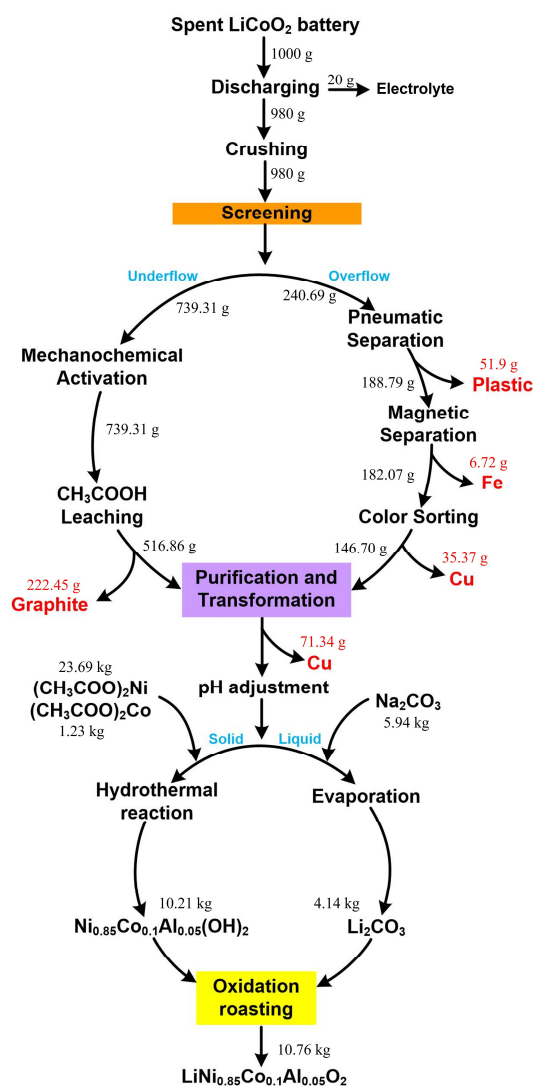
Figure S1 Data-quality flow chart of in situ upcycling of spent LCO batteries to prepare high-performance NCA batteries.
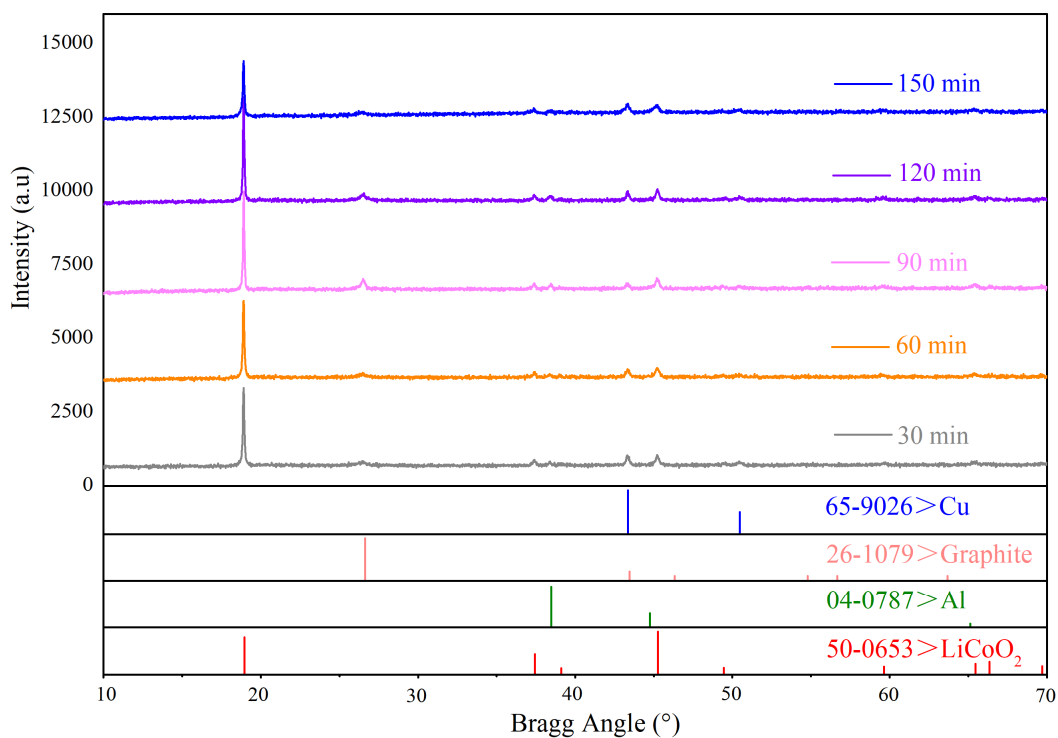
Figure S2 Lattice evolution process of crushed products of spent lithium ion batteries at different grinding times
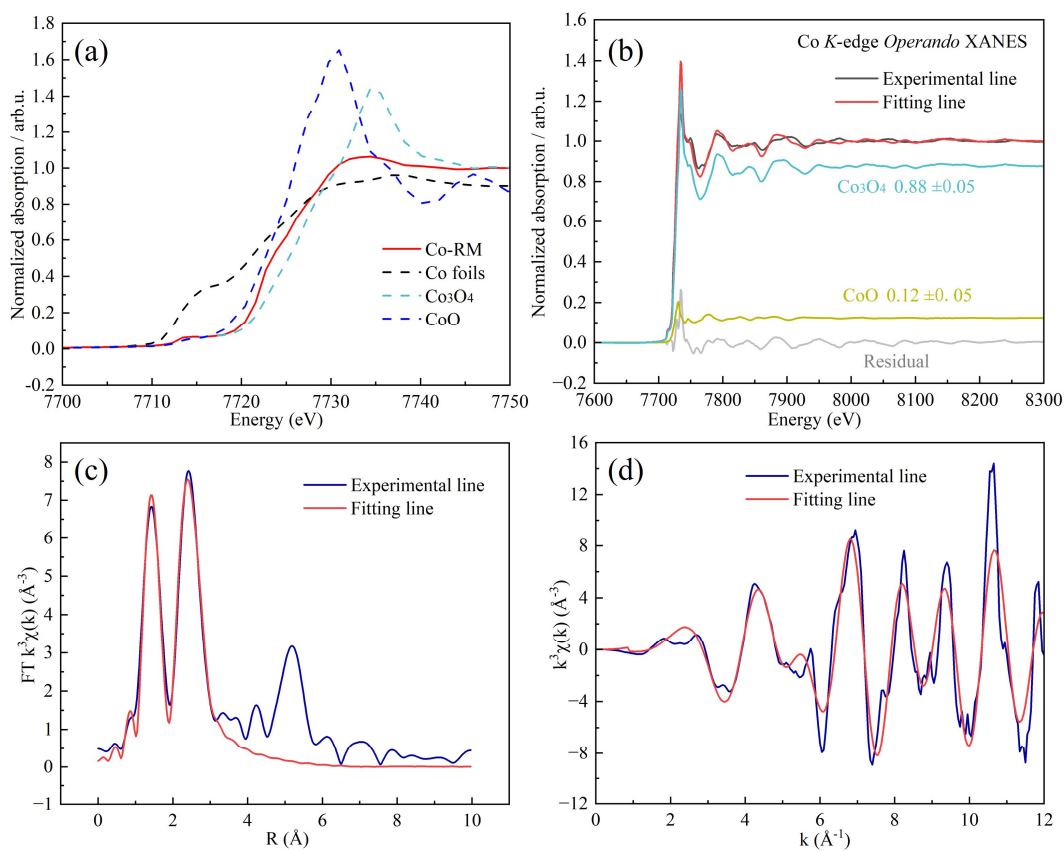
Figure S3 XAFS results of the raw materials from spent LCO cathodes (a. Co *K*-edge XANES of Co foils, CoO, Co₃O₄, and Co-RM; b. valence fitting analysis of Co atoms in Co-RM; c. fourier transform of EXAFS spectrum in R space and the best fitting result for Co-RM; d. fourier transform

of EXAFS spectrum in K space and the best fitting result for Co-RM)
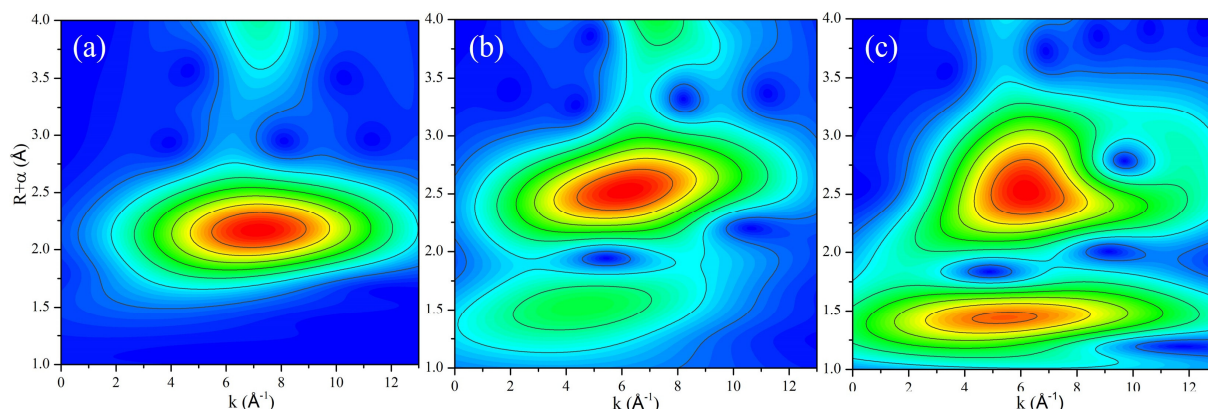
Figure S4 WT for the k^3-weighted EXAFS signals of (a) Co foil, (b) CoO and (c) Co_3O_4.

Table S1 EXAFS fitting parameters at the Co K-edge（S_0^2=0.76）

Sample	Path	C.N.	R (Å)	$\sigma^2 \times 10^3$ (Å²)	ΔE (eV)	R factor
Co foil	Co-Co	12*	2.49±0.01	6.2±0.1	8.2±0.2	0.001
CoO	Co-O	4.8±0.8	2.11±0.01	4.5±1.7	-0.5±1.8	0.004
	Co-Co	10.0±1.1	3.00±0.01	11.1±0.9	-4.8±1.0	
Co_3O_4	Co-O	4.4±0.5	1.92±0.01	1.3±0.8	-4.7±1.5	0.006
	Co-Co	4.2±1.6	2.87±0.02	3.2±2.2	-6.6±3.3	
	Co-Co	7.6±4.0	3.34±0.02	5.3±2.8	-10.6±3.0	
Co_2O_3	Co-O	5.4±0.7	1.92±0.01	3.0±0.9	-6.4±2.0	0.006
	Co-Co	4.7±1.5	2.86±0.01	4.0±1.8	-8.6±2.8	
	Co-Co	8.1±3.0	3.35±0.02	5.8±2.3	-9.1±2.7	
Co-RM	Co-O	3.0±0.6	1.90±0.01	2.2±2.1	2.9±2.3	0.007
	Co-Co	3.2±0.9	2.80±0.02	3.0±2.1	-1.7±2.7	
Co-MA	Co-O	3.2±1.0	1.94±0.02	2.9±3.6	-4.4±2.8	0.010
	Co-Co	7.0±4.2	2.43±0.04	48.0±11.6	6.0±3.1	

C.N.: coordination numbers; *R*: bond distance; σ^2: Debye-Waller factors; ΔE: the inner potential correction. *R* factor: goodness of fit. * fitting with fixed parameter. Co-RM means the raw materials from spent LCO batteries; Co-MA means the samples subjected to mechanochemical action.
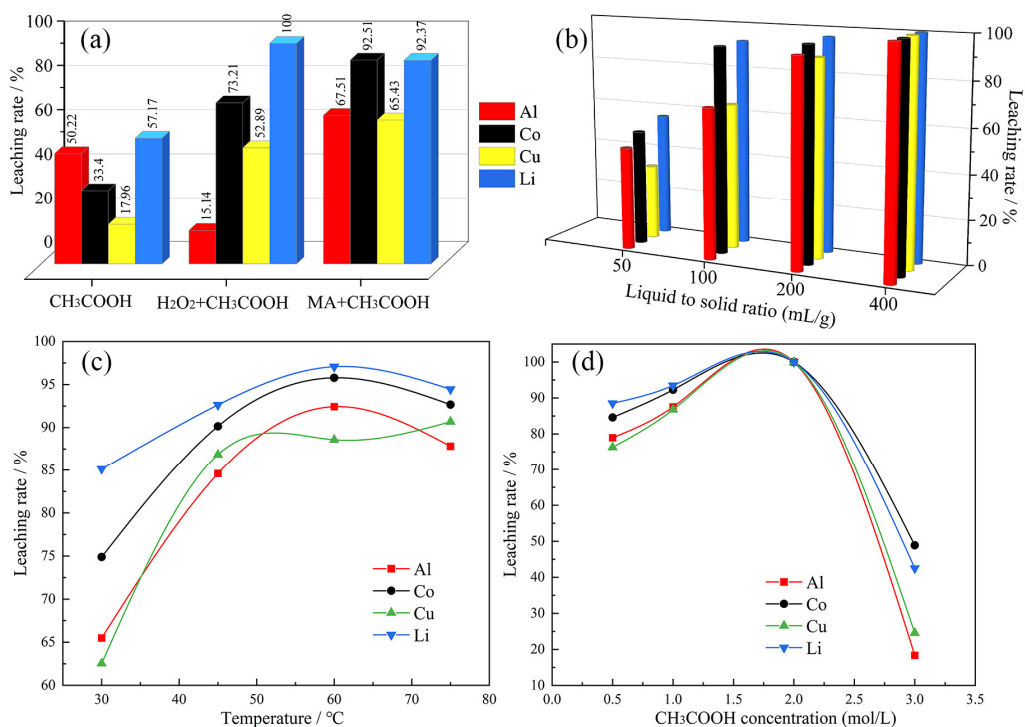
Figure S5 Verification and optimization of green leaching effect of in situ reduction products induced by mechanochemical force (a. verification of leaching effect, where MA means mechanical activation; b. leaching effect of different liquid-solid ratio; c. leaching effect at different temperatures; d. leaching effect of different acetic acid concentration).

Calculation method and process of E-pH curve. Aiming at the reactions between various substances in the recovery system, the curve equation of each reaction at specific temperature and concentration is calculated by using Gibbs free energy, Faraday's law and Nernst equation, and drawn on the same diagram to reveal the transformation between various objects in the system. The specific process is as follows.

For reaction:

$$mA + nH^+ + ze^- = bB + cH_2O$$
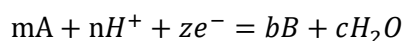
It can be derived from the Gibbs free energy formula and Nernst equation:

$$\Delta_r G_T = \Delta_r G_T^0 + RT \ln Q$$

$$E = E^0 - \frac{RT}{zF}\ln Q$$

Where R is the gas constant, F is the Faraday constant and T is the Kelvin temperature, $Q = \frac{a_B^b \times a_{H2O}^C}{a_A^m \times a_{H+}^n}$. Therefore, the functional relationship between reaction potential and pH of different reaction types (E-pH) can be further obtained:

(1) If $z \neq 0$, $m \neq 0$,

$$E = -\frac{\Delta_r G_T^0}{zF} - \frac{2.303RT}{zF}\log\frac{a_B^b}{a_A^m} - \frac{2.303RT}{zF}pH$$

(2) If $z = 0$,

$$pH = -\frac{\Delta_r G_T^0}{2.303nRT} - \frac{1}{n}\log\frac{a_B^b}{a_A^m}$$

(3) If $m = 0$,

$$E = -\frac{\Delta_r G_T^0}{zF} - \frac{2.303RT}{zF}\log\frac{a_B^b}{a_A^m}$$

The reaction equation and its corresponding parameters used in this study are as follows.

Reaction equation	T/K	E-pH expression
2H$^+$ + 2e$^-$ = H$_2$	298.15	E=-0.059pH
	363.15	E=-0.072pH
	423.15	E=-0.084pH
	473.15	E=-0.093pH
O$_2$ + 4e$^-$ +4H$^+$ = 2H$_2$O	298.15	E=1.229-0.059pH
	363.15	E=1.175-0.072pH
	423.15	E=1.127-0.084pH
	473.15	E=1.088-0.093pH
Cu^{2+} + 2e$^-$ = Cu	298.15	E=0.337
	363.15	E=0.337
	423.15	E=0.338
	473.15	E=0.340
Cu(OH)$_2$ + 2H$^+$ = Cu^{2+} + 2H$_2$O	298.15	pH=3.200
	363.15	pH=2.348
	423.15	pH=1.828
	473.15	pH=1.498
2Cu^{2+} + 2e$^-$ + H$_2$O = Cu$_2$O + 2H$^+$	298.15	E=0.211-0.059pH
	363.15	E=0.240-0.072pH
	423.15	E=0.265-0.084pH
	473.15	E=0.290-0.094pH
	298.15	E=0.463-0.059pH

$Cu_2O + 2H^+ + 2e^- = 2Cu + H_2O$	363.15	E=0.435-0.072pH
	423.15	E=0.410-0.084pH
	473.15	E=0.391-0.094pH
$2Cu(OH)_2 + 2H^+ + 2e^- = Cu_2O + 3H_2O$	298.15	E=0.590-0.059pH
	363.15	E=0.578-0.072pH
	423.15	E=0.572-0.084pH
	473.15	E=0.571-0.094pH
$CuO_2^{2-} + 2H^+ = Cu(OH)_2$	298.15	pH=17.539
	363.15	pH=15.491
	423.15	pH=14.351
	473.15	pH=13.774
$2\ CuO_2^{2-} + 6\ H^+ + 2e^- = Cu_2O + 3H_2O$	298.15	E=2.665-0.178pH
	363.15	E=2.811-0.216pH
	423.15	E=2.983-0.252pH
	473.15	E=3.157-0.282pH
$Al^{3+}+3e^-=Al$	298.15	E=-1.699
	363.15	E=-1.662
	423.15	E=-1.624
	473.15	E=-1.580
$Al(OH)_3+3H^+=Al^{3+}+3H_2O$	298.15	pH=3.772
	363.15	pH=2.523
	423.15	pH=1.710
	473.15	pH=1.116
$AlO_2^-+H_2O+H^+=Al(OH)_3$	298.15	pH=12.469
	363.15	pH=10.626
	423.15	pH=9.518
	473.15	pH=8.908
$Al(OH)_3+3H^++3e^-=Al+3H_2O$	298.15	E=-1.476-0.059pH
	363.15	E=-1.480-0.072pH
	423.15	E=-1.480-0.084pH
	473.15	E=-1.478-0.094pH
$Ni^{2+} + 2e^- = Ni$	298.15	E=-0.237
$Ni(OH)_2 + 2H^+ = Ni^{2+}+ 2H_2O$	298.15	pH=6.397
$Ni(OH)_3 + H^+ + e^- = Ni(OH)_2 + H_2O$	298.15	E=1.457-0.059pH
$Ni(OH)_3 + 3H^+ + e^- = Ni^{2+} + 3H_2O$	298.15	E=2.214-0.178pH
$Ni(OH)_2 + 2H^+ + 2e^- = Ni + 2H_2O$	298.15	E=0.142-0.059pH
$Mn^{2+} + 2e^- = Mn$	298.15	E=-1.182
$Mn(OH)_2 + 2H^+ = Mn^{2+} + 2H_2O$	298.15	pH=7.576

MnO*OH + H$^+$ + e$^-$ = Mn(OH)$_2$	298.15	E=0.504-0.059pH
MnO*OH + 3H$^+$ + e$^-$ = Mn^{2+} + 2H$_2$O	298.15	E=1.401-0.178pH
Mn(OH)$_2$ + 2H$^+$ + 2e$^-$ = Mn + 2H$_2$O	298.15	E=-0.773-0.059pH
Co^{2+} + 2e$^-$ = Co	298.15	E=-0.282
Co(OH)$_2$ + 2H$^+$ = Co^{2+} + 2H$_2$O	298.15	pH=6.193
Co(OH)$_3$ + H$^+$ + e$^-$ = Co(OH)$_2$ + H$_2$O	298.15	E=0.1.025-0.059pH
Co(OH)$_3$ + 3H$^+$ + e$^-$ = Co^{2+} + 3H$_2$O	298.15	E=1.758-0.178pH
Co(OH)$_2$ + 2H$^+$ + 2e$^-$ = Co + 2H$_2$O	298.15	E=-0.084-0.059pH
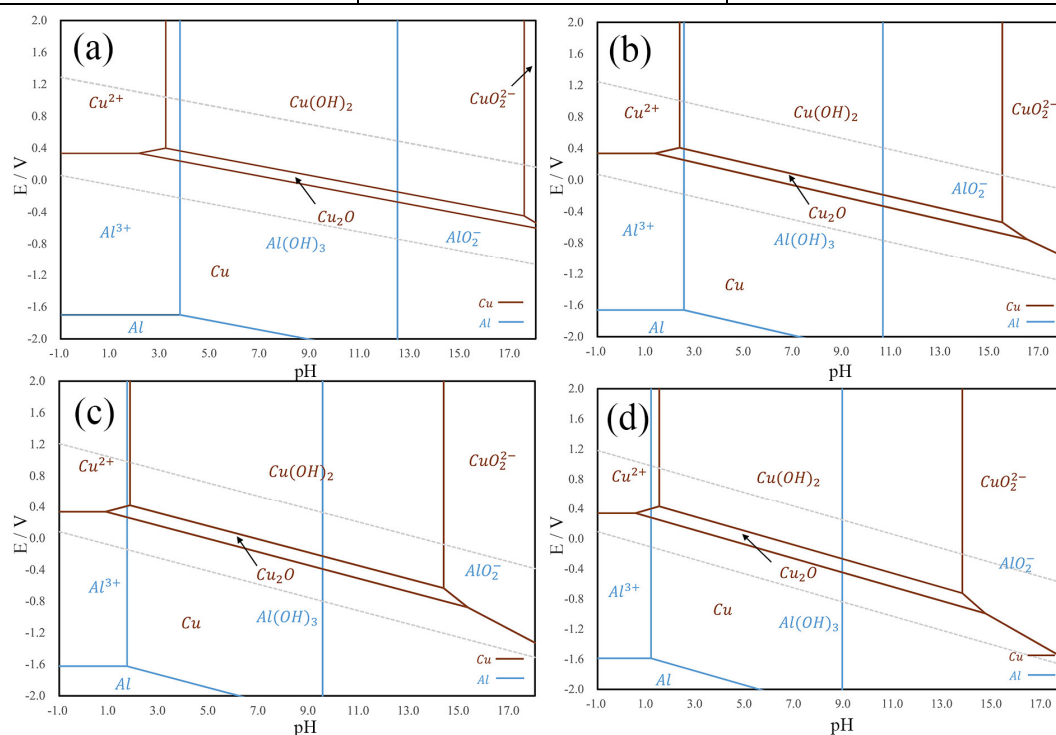
Figure S6 E-pH phase diagram of Al-Cu-H$_2$O system at different temperatures
(a. 298.15K; b. 363.15K; c.423.15K; d. 473.15K)

Table S2 Ion concentration in different batches of self-purification residual liquid

Element	Li(g/L)	Ni(g/L)	Co(g/L)	Mn(g/L)	Al(g/L)	Cu(g/L)	Fe(g/L)
a	0.78	0.12	5.86	0.09	2.38	0.00	0.01
b	0.69	0.08	5.99	0.05	2.45	0.00	0.01
c	0.85	0.07	5.88	0.12	2.55	0.00	0.01
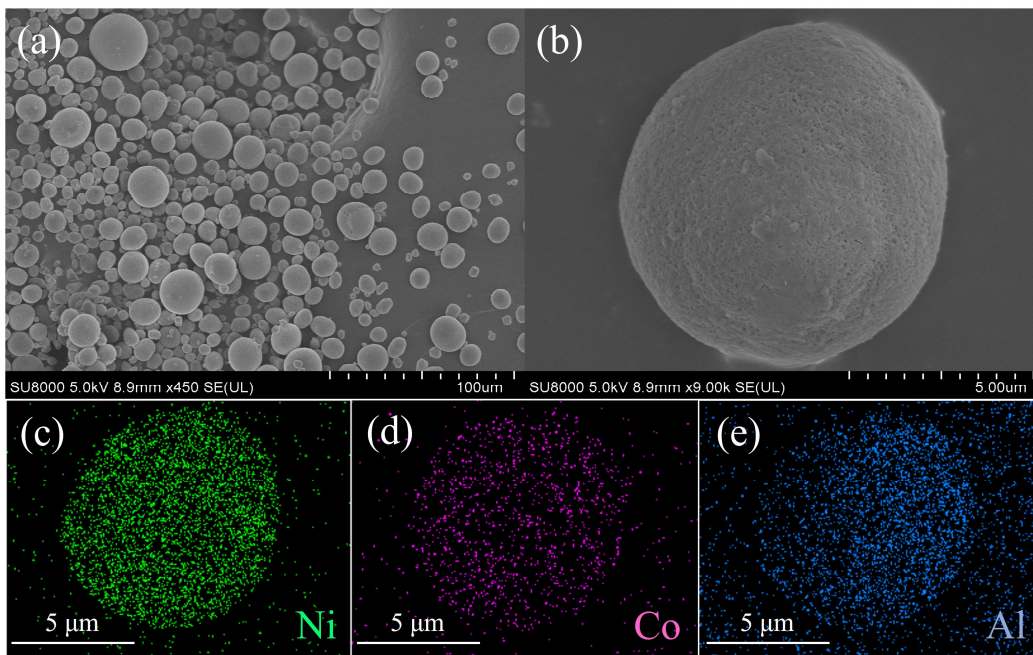
Figure S7 Micro morphology and element distribution of the NCA precursor
(a. micro morphology of the NCA precursor; b. micro morphology of a single NCA precursor particle; c. Ni distribution of the single particle in b; d. Co distribution of the single particle in b; e. Al distribution of the single particle in b)
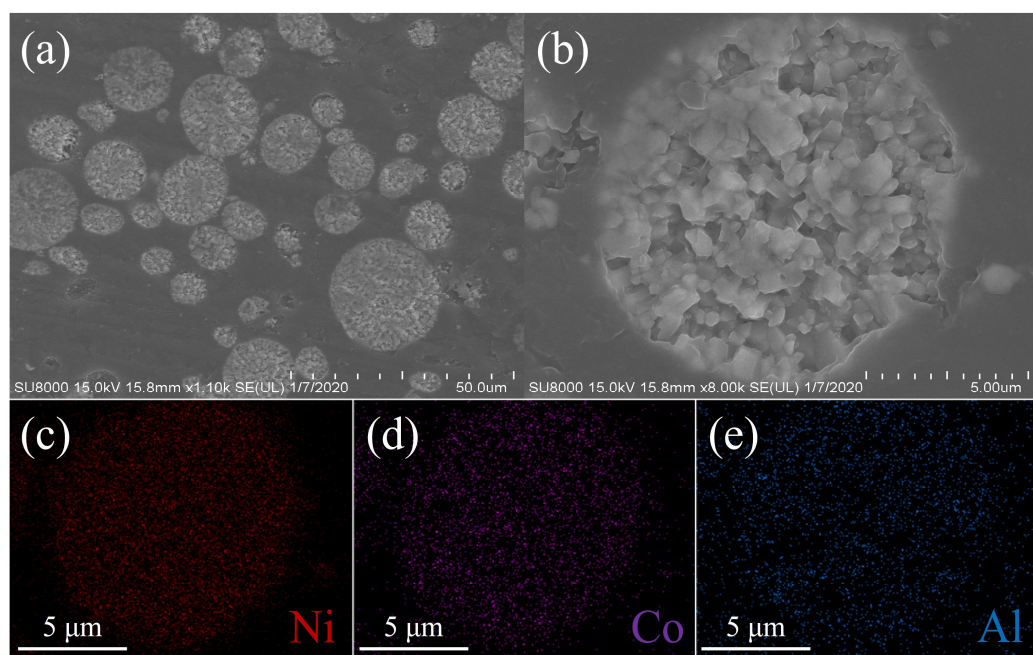
Figure S8 Micro morphology and element distribution of regenerated NCA cathode materials
(a. micro morphology of cross section of regenerated NCA cathode materials; b. cross-sectional micromorphology of a single regenerated NCA cathode particle; c. Ni distribution of the single particle in b; d. Co distribution of the single particle in b; e. Al distribution of the single particle in b)

Table S3 Lattice parameters of regenerated NCA cathode materials

Sample	a (Å)	b (Å)	c (Å)	Volume/ Å^3	c/a	I_{003}/I_{104}	Ni in Li site/%
NCA	2.874	2.874	14.191	101.500	4.937	2.412	0.916
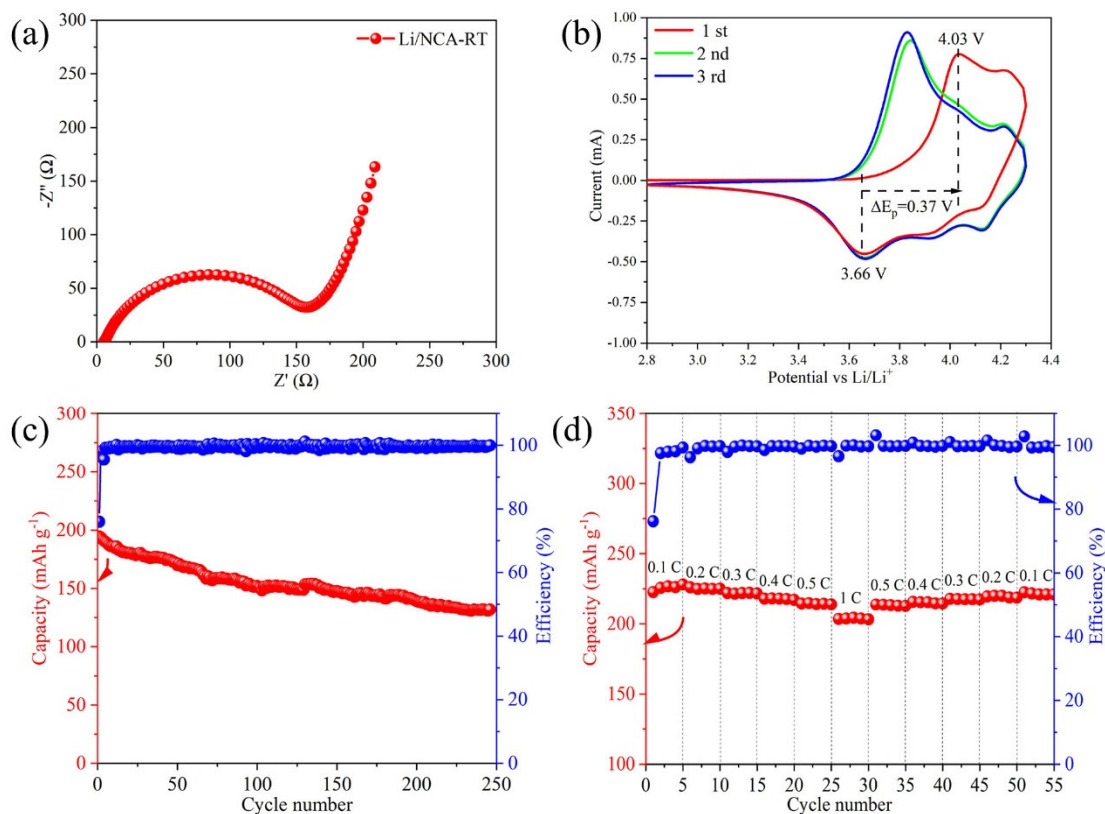
Figure S9 Electrochemical performance of commercial NCA cathodes (a. electrochemical impedance spectroscopy; b. cyclic voltammetry curve; c. battery cycle performance at 0.2 C; d. battery rate performance)

Data list of life cycle assessment method. GaBi is product system modeling and assessment software that first appeared on the market in 1992, developed and distributed worldwide by PE INTERNATIONAL, a German company. Gabi's built-in database contains thousands of types of substances, basic flows, energy and material processes, which can be used for life cycle research of various product systems. In addition, Gabi also includes a variety of environmental impact assessment methods such as CML 2001, Eco-indicator 99, ReCiPe 2016, TRACI, etc.. Among them, CML 2001 is the most commonly used evaluation method, which can quantify the relationship chain between

various modules in the early stage of modeling. The analysis results are based on traditional life cycle analysis features and standardized methods, thus reducing the number of installations and the complexity of the model. Therefore, this study uses CML 2001 as the environmental impact assessment method. The data list of conventional recycling process are as follows.

Step	Input	Dosage	Unit	output	Dosage	Unit	Product or waste	How to dispose
Safe discharging	Spent LIBs	1	kg	Discharged LIBs	0.98	kg		
	NaCl	5	g	NaCl	5	g		
	H$_2$O	100	g	H$_2$O	100	g		
	Electric	0.25	kWh	Electrolyte	20	g	Waste	Landfill
Double crushing	Discharged LIBs	0.98	kg	Crushing products	0.98	kg		
	Electric	3	kWh					
Deep screening	Crushing products	0.98	kg	Overflow products	601.33	g		
	Electric	5	kWh	Underflow products	378.67	g		
Air separation	Overflow products	601.33	g	Diaphragm	51.90	g	Waste	Burn
	Electric	0.75	KWh	Residual product (1)	549.43	g		
Magnetic separation	Residual product (1)	549.43	g	Coarse iron powder	12.99	g	Product	Sale
	Electric	0.75	kWh	Residual product (2)	536.44	g		
Color selection	Residual product (2)	536.44	g	Coarse Al powder	142.55	g	Product	Sale
				Coarse Cu powder	104.41	g	Product	Sale
	Electric	0.75	kWh	Electrode powder	289.48	g	Waste	Landfill
Alkali leaching	Underflow products	378.67	g	Alkali leaching residue	370.12	g		
	NaOH	40	g	Leaching solution	1048.55	g	Waste	Landfill
	H$_2$O	1	L					
	Electric	1.2	KWh					

Step	Input	Dosage	Unit	output	Dosage	Unit	Product or waste	How to dispose
Acid leaching	Alkali leaching residue	370.12	g	Graphite precipitation	132.67	g	Product	Sale
	H_2SO_4	345.72	g	Filtrate (1)	2731.27	g		
	Na_2SO_3	148.10	g					
	H_2O	2	L					
	Electric	1.2	KWh					
Impurity removal	Filtrate	2731.27	g	Impurity precipitation	13.42	g	Waste	Landfill
	NaOH	40	g	Filtrate (2)	3757.85	g		
	H_2O	1	L					
	Electric	1.2	KWh					
Co-precipitation	Filtrate (2)	3757.85	g	Precursor	1441.83	g	Product	Sale
	$LiAlO_2$	64.76	g	Li_2CO_3	124.55	g	Product	Sale
	$NiSO_4 \cdot H_2O$	3293.5	g	Na_2SO_4	2280.45	g	Product	Sale
	NaOH	1285.2	g	H_2O	6809.03	g	Waste	Circulate
	Na_2CO_3	124.55	g					
	H_2O	2.13	L					
	Electric	33	KWh					
Calcination	Precursor	1441.83	g	Cathode materials	1505.57	g	Product	Sale
	Li_2CO_3	578.93	g	CO_2	344.74	g	Waste	To air
	Electric	16	kWh	H_2O	170.45	g	Waste	To air

List of synthesis methods of $NaAlO_2$.

Step	Input	Dosage	Unit	output	Dosage	Unit	Product or waste	How to dispose
High temperature melting	Al_2O_3	101.96	g	$NaAlO_2$	163.94	g		
	NaOH	80	g	H_2O	18	g	Waste	To air
	Electric	16	kWh					

List of synthesis methods of Na_2SO_3.

Step	Input	Dosage	Unit	output	Dosage	Unit	Product or waste	How to dispose
Burning sulfur	S	32	g	SO_2	64	g	Waste	To air
	O_2	32	g					

Step	Input	Dosage	Unit	output	Dosage	Unit	Product or waste	How to dispose
	Electric	3	KWh					
Heating and stirring	NaOH	40	g	$NaHSO_3$	1104	g		
	SO_2	64	g					
	H_2O	1	L					
	Electric	4	kWh					
Evaporative crystallization	$NaHSO_3$	1104	g	Na_2SO_3	126.04	g		
	NaOH	40	g	H_2O	1017.96	g	Waste	To air
	Electric	8	KWh					

List of synthesis methods of Na_2SO_4.

Step	Input	Dosage	Unit	output	Dosage	Unit	Product or waste	How to dispose
Mixed + evaporative crystallization	H_2SO_4	98	g	Na_2SO_4	142.04	g		
	NaOH	80	g	H_2O	4035.96	g	Waste	Circulate
	H_2O	4	L					
	Electric	8	kWh					

The data list of new in-situ recycling process are as follows.

Step	Input	Dosage	Unit	output	Dosage	Unit	Product or waste	How to dispose
Safe discharging	Spent LIBs	1	kg	Discharged LIBs	0.98	kg		
	NaCl	5	g	NaCl	5	g		
	H_2O	100	g	H_2O	100	g		
	Electric	0.25	kWh	Electrolyte	20	g	Waste	Landfill
Single crushing	Discharged LIBs	0.98	kg	Crushing products	0.98	kg		
	Electric	1	kWh					
Mild screening	Crushing products	0.98	kg	Overflow products	240.69	g		
	Electric	0.5	kWh	Underflow products	739.31	g		
Air separation	Overflow products	240.69	g	Diaphragm	51.9	g	Waste	Burn
	Electric	0.75	KWh	Residual product (1)	188.79	g		
Magnetic separation	Residual product (1)	188.79	g	Coarse iron powder	6.72	g	Product	Sale
	Electric	0.75	kWh	Residual product (2)	182.07	g		
Color selection	Residual	182.07	g	Crude copper	35.37	g	Product	Sale

	product (2)							
				Electrode powder	36.61	g	Waste	Landfill
	Electric	0.75	kWh	Crude aluminum	110.09	g		
Mechanical activation	Underflow products	739.31	g	Activated products	739.31	g		
	Electric	4	KWh					
Acid leaching	Activated products	739.31	g	Graphite precipitation	222.45	g	Product	Sale
	CH₃COOH	723.6	g	Leaching solution	9240.46	g		
	H₂O	8	L					
	Electric	1.2	kWh					
Purification	Crude aluminum	110.09	g	Fe(OH)₃	11.45	g	Product	Sale
	Leaching solution	9240.46	g	Cu	71.34	g	Product	Sale
	Electric	1	KWh	NaAlO₂	459.03	g	Product	Sale
				Filtrate	8832.51	g		
Co-precipitation	Filtrate	8832.51	g	Precursor	2466.08	g		
	Nickel acetate	3790.16	g	Li₂CO₃	148.52	g	Product	Sale
	NaAlO₂	109.84	g	Sodium acetate	4506.73	g	Product	Sale
	NaOH	2036.8	g	H₂O	27861.04	g	Waste	Circulate
	Na₂CO₃	213.06	g					
	H₂O	20	L					
	Electric	28	KWh					
Calcination	Precursor	27861.04	g	Cathode materials	2574.94	g	Product	Sale
	Li₂CO₃	990.13	g	CO₂	589.6	g	Waste	To air
	Electric	32	kWh	H₂O	25.69	L	Waste	To air

List of synthesis methods of Nickel acetate.

Step	Input	Dosage	Unit	output	Dosage	Unit	Product or waste	How to dispose
Mixing and stirring	NiSO₄	154.76	g	Na₂SO₄	142.04	g	Waste	Landfill
	Na₂CO₃	105.99	g	NiCO₃	118.71	g		
	H₂O	2	L	H₂O	2000	g	Waste	Circulate

Step	Input	Dosage	Unit	output	Dosage	Unit	Product or waste	How to dispose
	Electric	1	kWh					
Evaporative crystallization	$NiCO_3$	118.71	g	Nickel acetate	176.78	g	Product	Sale
	Acetate	120.1	g	CO_2	44	g	Waste	To air
	H_2O	2	L	H_2O	2018.03	g	Waste	To air
	Electric	4	kWh					

List of synthesis methods of Cobalt acetate.

Step	Input	Dosage	Unit	output	Dosage	Unit	Product or waste	How to dispose
Mixing and stirring	HNO_3	168	g	$Co(NO_3)_2$	2206.93	g		
	Co	58.93	g					
	H_2O	2	L	NO	20	g	Waste	To air
	Electric	1	kWh					
Hot stirring	$Co(NO_3)_2$	2206.93	g	$CoCO_3$	118.94	g		
	Na_2CO_3	105.99	g	$NaNO_3$	169.99	g	Waste	
	Electric	1	KWh	H_2O	2023.99	g	Waste	
Acidification	$CoCO_3$	118.94	g	Cobalt acetate	177.02	g	Product	Sale
	Acetic acid	120.1	g	CO_2	44	g	Waste	To air
	H_2O	2	L	H_2O	2018.02	g	Waste	To air
	Electric	1	KWh					

In this study, the coupling method of material flow and life cycle economic analysis is used to complete the technical economic analysis of innovative methods. The economic value and quantity quality parameters of each step are shown in the following table.

Input list of industrial electricity:

Input	Recycling steps	Dosage / KWh	Cost price / RMB Yuan
Industrial electricity	Crushing and screening	1.75	2.625
	Separation and enrichment	2.25	3.375
	Mechanical activation	4	6
	Acid leaching	1.2	1.8
	Purification	1	1.5

	Co-precipitation	28	42
	Oxidation roasting	32	48
Total			105.3

Input list of industrial water:

Input	Recycling steps	Dosage / L	Cost price / RMB Yuan
Industrial water	Crushing and screening	0.1	0.00041
	Separation and enrichment		
	Mechanical activation		
	Acid leaching	8	0.0328
	Purification		
	Co-precipitation	20	0.082
	Oxidation roasting		
Total			0.11521

Input list of chemical additives:

Input	Recycling steps	Dosage / g	Unit Price (Yuan/t)	Cost price / RMB Yuan
spent LIBs	Crushing and screening	1000	76700	76.7
	Separation and enrichment			
	Mechanical activation			
CH$_3$COOH	Acid leaching	723.6	4200	3.03912
	Purification			
Nickel acetate	Co-precipitation	16829.456	79805.17027	1343.077602
Cobalt acetate		1226.7486	149418.5922	183.2990488
NaOH		8959.104	2500	22.39776
Li$_2$CO$_3$	Oxidation roasting	3980.08	480000	1910.4384
Total				3538.95

Output list of recycled products:

Recycling steps	Output	Dosage / g	Unit Price (Yuan/t)	Cost price / RMB Yuan
Crushing and screening				
Separation and enrichment	Diaphragm	51.9	5012	0.2601228
	Coarse iron powder	6.72	4000	0.02688
	Cu	35.37	56050	1.9824885
Mechanical activation				

Acid leaching	Graphite	222.45	42500	9.454125
Purification	Fe(OH)$_3$	11.45	4500	0.051525
	Cu	71.34	56050	3.998607
Co-precipitation	Sodium acetate	9187.36	3200	29.399552
Oxidation roasting	NCA cathodes	10759.8176	395500	4255.507861
Total				4300.68

In the above analysis, some special chemical additives and recycled products cannot be directly purchased in the raw material supply market, so we use the life cycle economic evaluation method to construct their actual price parameters.

The production cost of nickel acetate is calculated as follows. The results show that the unit production cost of nickel acetate is 79,805.17027 yuan/t.

Step	Input	Dosage	Unit	unit-price	Unit	cost/yuan	output	Dosage	Unit
Mixing and stirring	NiSO$_4$	154.76	g	38100	yuan/t	5.8964	Na$_2$SO$_4$	142.04	g
	Na$_2$CO$_3$	105.99	g	1800	yuan/t	0.1908	NiCO$_3$	118.71	g
	H$_2$O	2	L	4.1	yuan/m^3	0.0082	H$_2$O	2000	g
	Electric	1	kWh	1.5	yuan/KWh	1.5000			
Evaporative crystallization	NiCO$_3$	118.71	g				Nickel acetate	176.78	g
	Acetate	120.1	g	4.2	yuan/kg	0.5044	CO$_2$	44	g
	H$_2$O	2	L	4.1	yuan/m^3	0.0082	H$_2$O	2018.03	g
	Electric	4	kWh	1.5	yuan/KWh	6			

The production cost of cobalt acetate is calculated as follows. The results show that the unit production cost of cobalt acetate is 76,307.3777 yuan/t.

Step	Input	Dosage	Unit	unit-price	Unit	cost/yuan	output	Dosage	Unit
Mixing and stirring	HNO$_3$	168	g	1200	yuan/t	0.2016	Co(NO$_3$)$_2$	2206.93	g
	Co	58.93	g	61000	yuan/t	3.59473			
	H$_2$O	2	L	4.1	yuan/m3	0.0082	NO	20	g
	Electric	1	kWh	1.5	yuan/KWh	1.5			
Hot stirring	Co(NO$_3$)$_2$	2206.93	g				CoCO$_3$	118.94	g
	Na$_2$CO$_3$	105.99	g	1800	yuan/t	0.190782	NaNO$_3$	169.99	g

	Electric	1	KWh	1.5	yuan/KWh	1.5	H_2O	2023.99	g
Acidification	$CoCO_3$	118.94	g				Cobalt acetate	177.02	g
	Acetic acid	120.1	g	4.2	yuan/kg	0.50442	CO_2	44	g
	H_2O	2	L	4.1	yuan/m3	0.0082	H_2O	2018.02	g
	Electric	4	KWh	1.5	yuan/KWh	6			

The production cost of cobalt acetate is calculated as follows. The results show that the unit production cost of cobalt acetate is 149,418.5922 yuan/t.

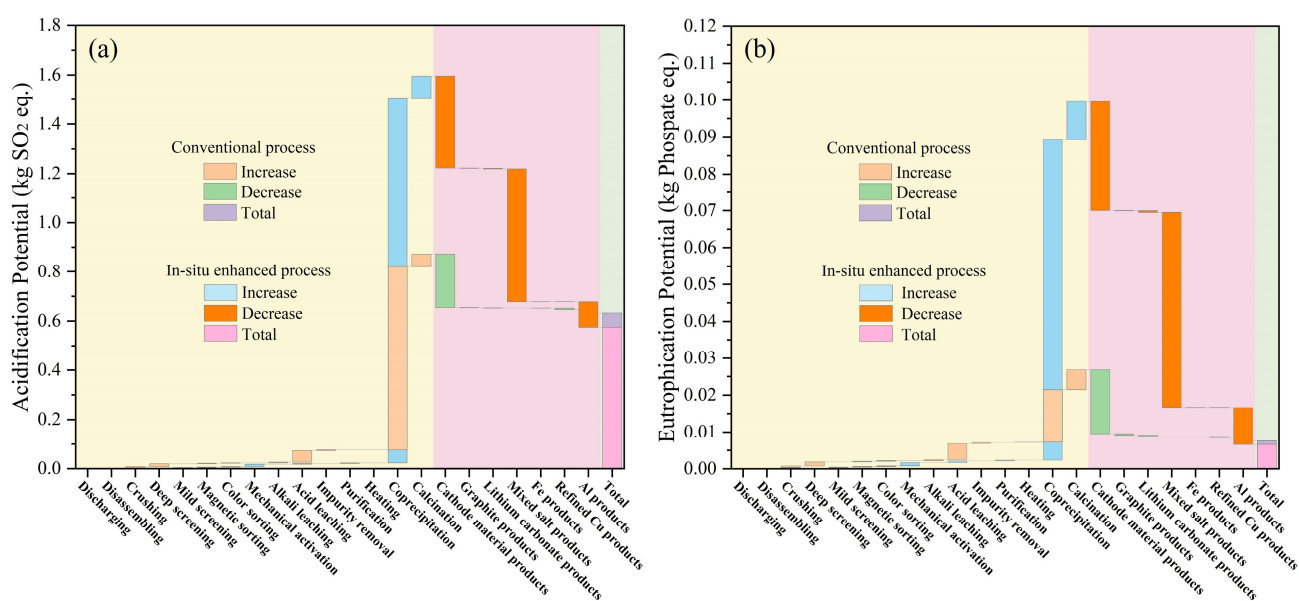| Step	Input	Dosage	Unit	unit-price	Unit	cost/yuan	output	Dosage	Unit
High temperature melting	Al_2O_3	101.96	g	2900	yuan/t	0.295684	$NaAlO_2$	163.94	g
	NaOH	80	g	2500	yuan/t	0.2	H_2O	18	g
	Electric	16	kWh	1.5	yuan/KWh	24			

Figure S10 Comparison of environmental impact between green upcycling process and conventional process for recycling spent lithium-ion batteries based on life cycle assessment (a. acidification potential; b. eutrophication potential)